5-11-2018

High Resolution Imaging and Digital Characterization of Skin Pathology By Scanning Acoustic Microscopy

Sarah Youssef
University of Windsor

Follow this and additional works at: https://scholar.uwindsor.ca/etd

High-Resolution Imaging and Digital Characterization of Skin Pathology by Scanning Acoustic Microscopy

By

Sarah Youssef

A Thesis
Submitted to the Faculty of Graduate Studies
through the Department of Physics
in Partial Fulfillment of the Requirements for
the Degree of Master of Science
at the University of Windsor

Windsor, Ontario, Canada

2018

High Resolution Imaging and Digital Characterization of Skin Pathology by Scanning Acoustic Microscopy

by

Sarah Youssef

APPROVED BY:

_____

A. Hubberstey
Department of Biological Sciences

_____

W. Kedzierski
Department of Physics

_____

R. Maev, Advisor
Department of Physics

May 9, 2018

DECLARATION OF ORIGINALITY

I hereby certify that I am the sole author of this thesis and that no part of this thesis has been published or submitted for publication.

I certify that, to the best of my knowledge, my thesis does not infringe upon anyone's copyright nor violate any proprietary rights and that any ideas, techniques, quotations, or any other material from the work of other people included in my thesis, published or otherwise, are fully acknowledged in accordance with the standard referencing practices. Furthermore, to the extent that I have included copyrighted material that surpasses the bounds of fair dealing within the meaning of the Canada Copyright Act, I certify that I have obtained a written permission from the copyright owner(s) to include such material(s) in my thesis and have included copies of such copyright clearances to my appendix.

I declare that this is a true copy of my thesis, including any final revisions, as approved by my thesis committee and the Graduate Studies office, and that this thesis has not been submitted for a higher degree to any other University or Institution.

ABSTRACT

Skin cancer represents the most common worldwide malignancy with a widely varying prognosis. Most of the diagnostic tools used for skin imaging are still limited to provide a definite diagnosis of skin cancer, especially melanoma. Easy access to the skin to biopsy and excision made skin underexplored using ultrasonic diagnostic imaging. Given the fact that speed of sound and acoustic impedance are related to elastic modulus, quantitative acoustic microscopy shows great potential as a useful tool for skin cancer diagnosis. The high-frequency acoustic microscopy method was used to evaluate properties of the cancer lesions for melanoma, basal cell carcinoma, and squamous cell carcinoma. The algorithm for quantitative characterization of individual cells in the histological slices has been developed. All cancer cells regardless of the cancer type have lower sound speed comparing to healthy skin cells. The melanoma cells have the lowest values of sound speed (1360 ± 50 m/s) comparing to basal cell carcinoma and squamous cell carcinoma. It was demonstrated on thickly cut skin specimens that melanoma lesions have lower acoustic impedance compared to healthy skin. These findings may become the basis for a new ultrasonic method for melanoma diagnosis or for margin status verification during the surgery helting to reduce the mortality rate from melanoma and improve healthcare in Canada and worldwide.

I dedicate my thesis to my loving family.

ACKNOWLEDGEMENTS

TABLE OF CONTENTS

LIST OF TABLES

LIST OF FIGURES

LIST OF ABBREVIATIONS

ABCDE	Asymmetry, Border, Colour, Diameter, Evolving
AM 50SI	Acoustic Microscope 50SI
AOS	Attenuation of Sound
AI	Acoustic Impedance
AC	Abnormal Squamous Cells
BCC	Basal Cell Carcinoma
BC	Basaloid Cell
B to Z	Brightness to Acoustic Impedance
BCC	Basal Cell Carcinoma
CM	Confocal Microscopy
CLSM	Confocal Laser Scanning Microscopy
dB	Decibel
E	Epidermis
HF	Hair Follicle
H&E	Hematoxylin and Eosin
HFUS	High-Frequency Ultrasound
KP	Keratinous Pearl
MRI	Magnetic Imaging Resonance
MM	Malignant Melanoma
NMSC	Non-Melanoma Skin Cancer
OCT	Optical Coherence Tomography
PVDF	Polyvinylidene Fluoride

PS	Polystyrene
PBS	Phosphate-Buffered Saline
PD	Papillary Dermis
P	Papillae
RI	Refractive Index
ROI	Region of Interest
REB	Research Ethics Board
RCM	Reflectance Confocal Microscopy
RD	Reticular Dermis
T1	Spin-Lattice Relaxation Time
T2	Spin-Spin Relaxation Time
SAM	Scanning Acoustic Microscope
SC	Stratum Corneum
SG	Stratum Granulosum
SS	Stratum Spinosum
SB	Stratum Basale
SCC	Sqaumous Cell Cracinoma
SOS	Speed of Sound
SD	Standard Deviation
3D	Three-dimensional
US	Ultrasonography
WRH	Windsor Regional Hospital
ZnO	Zinc Oxide

LIST OF SYMBOLS

δ_{axial}	Axial Resolution [m]
L	Amplitude of the reflected wave [dB]
Z	Acoustic impedance [Rayl]
α	Absorption coefficient [dB/m]
K	Bulk modulus [Pa]
ρ	Density [kg/m^3]
D	Diameter Aperture [m]
z	Distance from the transducer [m]
h	Edge thickness of the lens [m]
E	Elastic modulus [Pa]
f_0	Focal length [m]
F	F-number of the lens
f	Frequency [Hz]
θ	Half aperture angle
N	Length of Fresnel region [m]
$\delta_{lateral}$	Lateral Resolution [m]
n	Non-negative integer
σ	Poisson ratio
ϕ	Phase angle [degrees]
R	Radius of curvature [m]
r	Radius of the lens [m]
$\bar{c}$	Refractive index

c	Speed of sound [m/s]
A	Slope of attenuation [dB/m. Hz]
S	Signal amplitude [dB]
G	Shear modulus [Pa]
P	Sound power [W]
η_s	Shear viscosity [Pa.s]
v_s	Sound velocity in Buffer Rod [m/s]
δ	Thickness of the crystal [m]
d	Thickness of the tissue [m]
η_v	Volumetric viscosity [Pa.s]
λ	Wavelength [m]

CHAPTER 1

INTRODUCTION: SKIN STRUCTURE AND SKIN CANCER

1.1 Structure and Function of the Skin

Human skin is the largest organ in the body, accounting for approximately 16% of total body weight [1]. It has many functions. One of the most important is to protect the body from external aggressions (injuries, infections, ultraviolet radiation and water loss). It is a highly organized complex tissue composed of several distinct layers and components. The three primary layers are the epidermis, the dermis, and the hypodermis.

The superficial layer, the epidermis, is a stratified squamous epithelium layer consists of four types of cells. The predominant type is the keratinocytes (95%) [2] which are formed by the division of cells in the basal layer of the epidermis. They produce keratins that are the major structural proteins of the outer layer of the epidermis known as stratum corneum or horny layer. Deep in the epidermis are cells called melanocytes. Melanocytes make melanin pigment source for skin and hair colour.

Below the epidermis is the dense fibroelastic connective tissue layer, the dermis. It is mainly made of collagen and elastin fibres which exhibits the viscoelasticity behaviour of the skin. These proteins are synthesized by fibroblasts cells that formed the most numerous dermal cells. Also, it contains blood and lymph vessels, nerve endings and skin appendages such as hair follicles, sebaceous and sweat glands. Its vital role is to provide energy and nutrition to the epidermis and to regulate the temperature of the body. The dermis comprises of two sub-layers, the papillary dermis (thin layer) and the reticular dermis (thick layer).

The third layer is the hypodermis, called as well subcutaneous fat, lies immediately under the dermis layer. It contains loose fatty connective tissue, and it is used mainly for fat storage. Thus, adipocyte cells represent a large number of cells in the hypodermis.

There are two main kinds of human skin, glabrous skin, and hairy skin. The first is found on the palms and soles with a relatively thick epidermis and lack of hair follicles. However, hair follicles are present in the hairy skin.
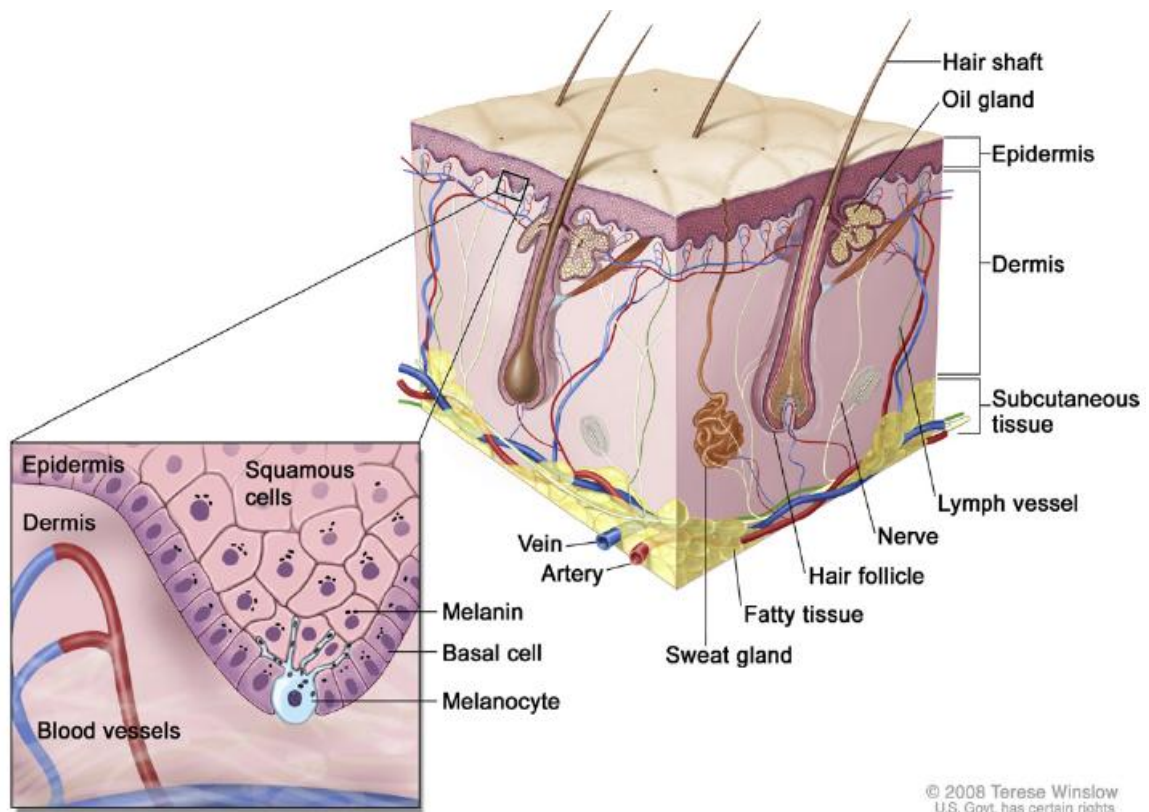
Figure 1.1: Anatomy of the skin showing main layers with their essential constituents [2].

1.2 Skin Cancer

Skin cancer is a group of cancers with increasing incidence rate that appears predominantly in Caucasian and elder people yielding to increase the incidence of mortality and therapeutic expenses as a burden to the health-care system [3]. The most common malignant skin tumours are composed of two categories: malignant melanoma (MM) and non-melanoma skin cancer (NMSC) with different diagnostic types. In this study, we will consider keratinocyte types of non-melanoma skin cancers, basal cell carcinoma and squamous cell carcinoma, as they relate to 99% of skin cancer cases [4], [5] along with cutaneous melanoma as it relates to 90% of deaths associated with skin cancer [6].

1.2.1 Basal Cell Carcinoma

Basal cell carcinoma (BCC) is the large common skin cancer type. It starts to develop in the basal cells of the epidermis at the basement membrane and proliferates into atypical basal keratinocytes known as basaloid cells [4]. They are typically surrounded by collagen fibres. Nevertheless, at progressive cancer stage, stroma in the dermis is reduced (about 30%) with the enlargement in size and number of tumour nests [7], [8]. These cancer clusters present various histological types of BCC depending on the different configuration of atypical cells. In the present study, superficial BCC was considered that is characterized by spreading of peripheral palisaded basaloid cells in the nest all over the epidermis with well-defined border [4].

BCC is typically diagnosed during a clinical examination with subsequent confirmation of the diagnosis by histopathological analysis. In spite of its low mortality rate, BCC can cause metastasis if kept untreated for a long-time and mainly if the first treatment was insufficient. BCC is associated with the excessive sunlight exposure and is treated by

surgical excision of a tumour with a large margin for advanced stage or by cryotherapy or laser therapy for superficial BCC [7], [9] .

1.2.2 Squamous Cell Carcinoma

Squamous cell carcinoma (SCC) is malignant cutaneous tumour that can metastases and cause death. Meanwhile, BCC could be invasive with normally not metastasizing while melanoma has a unique ability to metastasize very fast comparing to SCC [10]. The invasive type of SCC discussed in this study forms 20% of all skin malignancies [4], [11]. However, many different types of SCC exist and ranging from low to more aggressive attitude.

Usually, SCC originates from in situ neoplasms such as actinic keratosis, and Bowen's disease where it is characterized by the proliferation of squamous keratinizing cells through the epidermis and its appendages. For more invasive growth, these non-pigmented atypical cells infiltrate into the dermis as tumour clusters from further mutation. The tumour clusters are surrounded by reduced stroma with lymphocytes and are transformed later to keratinous pearls for the well-differentiated SCC type. Despite of that, keratinization is not always apparent what may leads to misdiagnosis of SCC with melanoma. Similarly to BCC, sun and ultraviolet light exposure are significant risk factors for SCC and particularly in the elderly population [12]. Also, SCC can develops from irradiated or inflamed skin [11].

1.2.3 Melanoma

Cutaneous malignant melanoma (MM) is the less frequent skin cancer that constitutes about 2% of cases [13]. However, it causes the vast majority of deaths comparing to non-melanoma skin cancer due to its rapid metastatic and malignancy characteristic [13]–[15].

It can vastly invade in the lymph node and over the body through the lymphatic and blood vessels [16] . It has the highest ability to be cured at an early stage that increases the five year survival rate to 95% [6]. Nevertheless, the early prognosis of MM is poor and presents clinical defiance for dermatologists because of the same features are seen in melanoma and in dysplastic or melanocytic nevi.

There are many subtypes of melanoma, but we focus on malignant melanoma in our study. Melanoma cells begin at the basal layer in the melanocytes that produce melanin. Those atypical melanocytes proliferate irregularly either as a single cell or as clusters along the epidermal-dermal junction and invade into the dermis with a different shape. Also, they can form a "Pagetoid" spread into the epidermis [17]. Environmental risk factors are related to the previous history of melanoma, and multiple moles in the body are associated with developing MM. Other factors are the ultraviolet and chemical exposure and from scars also [15].

1.3 Clinical Diagnosis of Skin Cancer

1.3.1 Visual Inspection

The primary skin assessment typically occurs at the primary points of care with the visual inspection as the most common type of evaluation. Although it is frequently used, naked eye examination poses some challenges in prognosis to differentiate between benign and malignant lesion [13]. Therefore, traditional biopsy or excision is required to confirm the diagnosis [6], [16]. The histopathology procedure increases the diagnosis as it provides a cellular and subcellular structures visualization.

1.3.2 Biopsy for Diagnosis Confirmation

Two types of biopsy are used depending on tumour size and treatment method. An incisional biopsy where a small piece of a tumour is cut out surgically by incision, punch or shave issued when the diagnosis is not certain. Otherwise, an entire removal of the lesion and some healthy tissue around it is carried out and is known as an excisional biopsy, followed by a preoperative assessment of the maximum tumour thickness measured with a micrometer on the histology slide [18]. Sometimes, the tumour shows many recurrent lesions and demands repetitive biopsy that could be limited by health conditions of the patient or by the lesion position.

Recently, Mohs surgery is suggested as a treatment for BCC and SCC clinically where the surgeons cut out a thin layer of a tumour with a surgical knife through local anesthesia and examine the tumour layer under a microscope during the surgery. This operation is repeated until no more cancer cells are seen in the removed tissue. The advantageous of this technique over the standard excision is the ability to save as much normal skin as possible around the lesion especially in the aesthetically and functionally critical sites (ear, face, feet, and finger). However, all these conventional methods for diagnosis are slow to process, required many hours to be completed, expensive, and present many risks for patients such as pain, infection, bleeding and medical care after surgery [2], [11], [19], [20].

1.3.3 Dermoscopy

A non-invasive technique called dermoscopy is used to enhance lesion visualization under the skin surface by combining oil immersion and light magnifying device and to prevent performing unnecessary biopsies. It is mostly applicable to pigmented skin cancer [2],

[20]–[22]. Nonetheless, dermoscopic images are still limited to use by skin artifacts (hair, oil bubbles, and skin structures) that create a disparate light. Also, the method requires additional training for the clinician [23], [24].

For melanoma diagnosis, ABCDE rule or 7-point checklist or Menzie rule is adopted by physicians. The ABCDE criteria of dermoscopy are mostly used in clinical practice as the simplest one where it is based on the Asymmetry, Border irregularity, Colour variegation, Diameter> 6mm and Evolving of the lesion [2], [13], [16], [17], [24].

The clinical appearance of SCC using dermoscopy can be detected with different diagnostic features such as white structures and circles, glomerular vessels that help to recognize this type of cancer. However, for invasive SCC non-keratotic type, different biological markers are used to avoid false negative diagnosis with BCC and to see tumour extension [11], [20].

1.4 Goals and Structure of the Thesis

The majority of skin cancer are underestimated that causes severe morbidity and increases in mortality rate [25]. Clinical assessment of the lesion by visual inspection is often not enough, and biopsy stays the standard diagnostic reference for diagnosis confirmation. Therefore, a diagnostic technology to support clinician's decision could potentially increase the accuracy and lower morbidity and mortality associated with MM.

Though the ultrasound is used for estimation of the tumour thickness of the primary melanoma, the diagnostic potential of the conventional ultrasound to identify specific skin pathologies is rather limited. Easy access to the skin for biopsy and excision made skin underexplored using ultrasonic diagnostic imaging. At the same time, numerical simulations and experimental studies show that malignant skin lesions including melanoma

have distinct elastic properties compared to benign lesions and healthy skin. As the speed of sound and acoustic impedance measured by the acoustic microscopy are the indirect measurements of the elastic modulus, it is worthwhile to explore if the high-resolution acoustic microscopy has the potential for identifying and classifying skin cancers.

This study aims: 1) to provide a methodology for high-resolution imaging of human skin using an acoustic microscopy method and to find a correlation of the ultrasonic images with traditional stained optical images, 2) quantitatively characterize acoustic properties of cancer neoplasms emphasizing significant features for diagnostics in daily practice.

The thesis is divided into six chapters. Chapter 1 describes the structure of skin and outline the major skin cancer types. Chapter 2 presents a complete literature review of the non-invasive skin imaging techniques and the proposed scanning acoustic microscope method. Chapter 3 offers the principle of scanning acoustic microscope, general description of the acoustic lens and the theory behind acoustic properties calculation. Chapter 4 illustrates the experimental setup and materials used. Chapter 5 displays the results and the analysis of acoustic properties of melanoma and non-melanoma comparing to normal and histopathology. Chapter 6 discusses the conclusions and future work.

CHAPTER 2

LITERATURE REVIEW: SKIN IMAGING METHODS

2.1 Non-Invasive Skin Imaging Methods

Many non-invasive skin imaging methods have been created in order to examine tissue in its native state in order to avoid biological biopsies and related timely preparation work. Thus, many selected skin sites will be monitored over time to visualize various skin lesion structures and their changes due to ageing and/or medication treatment. These modalities comprise ultrasonography, optical coherence tomography, confocal microscopy, and magnetic resonance imaging.

2.1.1 Ultrasonography

Ultrasonography (US) is an acoustic technique used to image vertical sections in the tissue. A gray scale image is obtained from the reflection of sound waves and depends on the difference in acoustic impedance and, therefore, on the acoustic properties of the tissue [26].

Conventional ultrasonic devices with a frequency ranging from 7.5 up to 15 MHz are used for measuring skin tumour thickness in clinical practice before the surgical excision as it appears hypoechogenic. However, in some cases, it's hard to determine the margins when the tumour exceeds the dermal layer and invades the subcutis that looks hypoechoic too [18], [27].

B-mode scanners with 20 MHz transducers are used in real-time mode to identify all skin layer morphology and cutaneous lesions. They can penetrate to a depth of 3.8 mm into the skin yielding to an axial and lateral resolution of approximately 39 µm and 210 µm,

respectively. In skin cancer, especially melanoma, the thickness is a prognostic factor for dermatologists. Several former studies for evaluation of skin lesions at this frequency (20 MHz) have shown that the thickness of melanocytic skin tumour (> 1mm) strongly agrees with histologic thickness while for thin (<1mm), it is considered overestimated comparing to Breslow thickness. The inflammatory infiltrate around the tumour is one of the causes that lead to overestimation [6], [18], [27]–[30]. This issue can be resolved by using higher frequency probes which have a higher resolution, although the resolution is inversely related to penetration depth.

It has been demonstrated that thickness of melanocytic and non-melanocytic skin cancer measured with 100-MHz US provide better correlation with histologic measurements than 20-MHz US with an axial and lateral resolution of 9.9 μm and 84 μm respectively [31]–[33]. High- frequency ultrasound (HFUS) can discriminate between basal cell carcinoma as it appears non-homogeneous with low defined pattern and melanoma where it shows homogeneous hypoechoic echo with well-delimited pattern [26], [27], [31], [34]–[37]. Also, BCC and SCC were able to be distinguished with HFUS by the presence of hyperechoic spots in the first carcinoma [26], [38]. However, HFUS is limited in the epidermis and upper dermis layers of the skin with a penetration depth of 1.1 mm but it is insufficient for thicker tumours [32]. New ultrasonic devices were combined with Doppler to increase the sensitivity to differentiate between melanoma and benign pigmented lesions by evaluation of tumour vascularization [18], [26].

In skin imaging, variations of ultrasonic reflections depend on tissue composition (keratin, water, and collagen) that displays different echoes in B-mode image [38].

Many quantitative ultrasonic methods were developed to provide additional information related to skin composition and intrinsically to visco-elastic characteristics since conventional ultrasound image is restricted [6], [8], [13], [24], [28], [39]–[42]. Among all acoustic parameters, frequency-dependent attenuation and backscatter coefficients are discriminating factors for specific tumour types [43]. Malignant melanoma is more attenuated than melanocytic nevi [6]. Also, highly keratotic cancer (BCC, SCC) is attenuated stronger than normal [40].

Also, for 20 to 30 MHz US, the speed of sound, attenuation and backscatter coefficients were calculated for epidermis and dermis layer of healthy human skin [40]. Ultrasound velocity rises with more collagen or keratin and decreases with more water content. A study on melanoma tissue demonstrates that sound speed is lower compared to human skin and ranging from 1553-1588 m/s [28].

Some works currently have shown the use of ultrasound elastography as a method to characterize skin cancers especially cutaneous melanoma, indicating that the melanoma lesion is stiffer than the surrounding tissue [44]. Malignant neoplasms offers very low elasticity comparing to benign lesions [38]. While HFUS is used to evaluate skin cancer especially malignant melanoma and BCC, it cannot provide cellular resolution, and therefore it cannot be used alone to confirm the diagnosis. Nevertheless, this is a safe, non-radioactive and non-expensive technique comparing to CM, MRI, and OCT.

2.1.2 Optical Coherence Tomography

Optical coherence tomography (OCT) is an interferometry method that provides lateral scanning high resolution two-dimensional cross-sectional images of the internal microstructure of living tissue. The concept behind low coherence tomography that the

light in the human skin is focused on the superficial skin layers, backscattered and recombined with the reflected reference signal from the scanning mirror. Coherent interference occurs only if the path length of both beams agree within the short coherence length of the light source. Therefore, the resolution of OCT system is determined by the coherence length and the power of the light source used, the focal spot size of the lens and the step width[45], [46]. It is mainly based on the emission of near-infrared light in the wavelength range from 700 nm to approximately 1300 nm where the absorption and scattering into the tissue are relatively low, especially in the human skin that is considered as a non-transparent and high scattering medium. So that light penetrates deep into the skin in the order of 1- 2 mm yielding to an axial and lateral resolution of approximately 15 μm much higher than that of 20 MHz transducers [47], [48]. Hence, at that detection depth only superficial layers of the skin could be visualized, and thus epidermal thickness could be measured easily. Also, in cross-sectional images, the dermo-epidermal junction in the skin could be sharply demarcated as well as adnexal structures and blood vessels. However, conventional OCT is not able to detect cellular details since multiple light scattering and a coherence length larger than most cell diameters [47], [49]–[52].

For thin NMSC, OCT could evaluate the tumour thickness that correlates well with histology thickness in all cases, especially for BCC [31]. Nevertheless, it is still less accurate than clinical diagnosis, and it is hard to differentiate between a benign and malignant tumour as well as cancer margins could not be delineated by OCT [20], [46], [48], [53], [54].

2.1.3 Confocal Microscopy

Real-time confocal microscopy (CM) is an optical imaging technique with high determination and contrast that shows horizontal planes of the skin surface without physically dissecting the tissue, to obtain the so-called 'optical sectioning'. Thus, a 3-D profile can be reconstructed by scanning and combining sequentially many confocal planes at different depths in the skin where it becomes comparable to the reconstruction of magnetic resonance and computed tomography images. This imaging technique is based on the emission of incoming light from a point source aperture or laser pulse that is focused by an objective lens in order to irradiate a small volume inside the tissue. The light from the illuminated spot is reflected back to the same objective and split from the excitatory light by a dichroic mirror. Unlike the conventional light microscopy, the resulting or fluorescent light is detected by a detector through a pinhole that operates as a spatial filter where only the light signal from the focal point is registered [55]–[58]. The quality of the confocal image is not only marked by resolution but also by contrast. So, signal contrast originates from the difference of the refractive index (RI) of various cell types and the size of organelles. In skin imaging, a strong signal is gathered specifically from keratin, melanin, and collagen that render a light contrast [56], [57], [59]. A remarkable advance in the optimization of the illumination and detection system of the CM is generated in order to improve confocal microscopy images quality of the human skin and to reduce scanning time. Therefore, the most useful and beneficial clinical one is confocal laser scanning microscopy (CLSM) that presents a high lightening power and a specific wavelength selectivity [57], [59]. With this method, the nuclear and cellular morphology of the human skin is provided at a resolution of 2 μm to a limited depth of 100- 200 μm where various

structures of the entire epidermis and part of the dermis can be clearly identified [60]. It shows dermal papillae, collagen fibres and blood cells flowing through the capillary loops of the papillary dermis as well as sweat ducts, sebaceous glands and hair follicles [56], [58], [59]. Also, the thicknesses of the different epidermal layers and the sizes of the cellular nuclei can be obtained. For melanocytic skin tumours imaging, CLSM can discriminates malignant melanoma from benign through the identification of morphological changes features that come to an accurate presurgical diagnosis and to determine their margins before biopsy [61]–[63]. For the diagnosis of BCC, a study has evaluated the clinical applicability of reflectance confocal microscopy (RCM) with high sensitivity. Limitations include the failure to visualize the depth invasion of skin tumours on horizontal sections and inability to evaluate lesions with significant hyperkeratosis. Nonetheless, the assessment of confocal images imposed a high training level and experience of the dermatologists and examining physician [56]. Another limitation, the expensive cost of CM and the inability to assess hyperkeratosis lesions [64]. Moreover, the vertical invasion of the lesion deeply into the skin cannot be evaluated reliably as CM detects horizontal section only in contrast to OCT, MRI and US technique [58][65].

2.1.4 Magnetic Resonance Imaging

Magnetic resonance imaging (MRI) is a technique that presents cross-sectional imaging analogous to optical and ultrasound techniques and reflects the bulk magnetic properties of the tissue by the use of radiowaves. The magnetic resonance image is obtained from the transition energy of atoms to their ground state and acquired by a surface receiver coil, especially the response of hydrogen atoms which are frequent in both fat and water.

In dermatology, 1.5 T MRI allowed the visualization of healthy skin structure and differentiate between skin layers in function of water contrast [66]–[68]. Different parameters such as T1 and T2 relaxation times, density of protons, gradient and spin echoes are evaluated by high resolution MRI technique for diagnosis of skin abnormalities that correlate well with histological findings. Therefore, for skin carcinomas (BCC and SCC), it provides information about the tumour morphology as well as it determines the margin and the depth of the tumour [20], [69], [70].

Other studies shows that it could be used for in-vivo to evaluate different melanoma types and detect metastasis stage in relation to the surrounding structures [67], [70], [71]. In contrast to ultrasound imaging, MRI potentially localized inflammatory infiltration into the dermis [68]. Although some studies shows the advantageous of MRI to assess tumor invasions equally to clinical findings, the diagnostic role is still limited comparing to CM, US, and OCT in addition to its very high cost.

2.1.5 Comparison of Skin Imaging Methods

While non-invasive imaging techniques may aid dermatologist in the diagnosis of melanoma and non-melanoma skin cancer, they pose several limitations. OCT, HFUS, and MRI lack the resolution to detect early stage skin cancers especially melanoma whereas RCM is not able to image in depth, therefore invasive SCC and other cancers cannot be detected. For that reason, there is still need for other imaging techniques providing high resolution for diagnosis of different skin cancers at the cellular level and help to select the appropriate treatment.

2.2 Scanning Acoustic Microscopy

The scanning acoustic microscopy (SAM) is a method that utilizes high-frequency focused sound waves to image an object and investigate its elastic properties. The sound wave is emitted from a transducer and focused at a small point on a target object. The sound is transmitted and reflected at the coupling/tissue interface and scattered and absorbed inside the tissue. The reflected signal is received by the transducer and analyzed. The transducer is moved along the sample to create the image. The contrast of the image is based on the specimen's stiffness, viscosity, morphology and geometry. This method permits the imaging not only the surface but also the internal structure of tissues. At the operating frequency in the range of several GHz, it has a sub-micron resolution comparable to an optical microscope [72]. Although the higher frequency provides higher spatial resolution image, the depth of visualization and signal level in this case dramatically reduced due to sound attenuation.

Lemons and Quate for the first time demonstrated in 1974 working acoustic microscope in the transmission mode and used it for biomedical applications [73]. This acoustic microscopy method was later extended theoretically and experimentally by observing various biological tissues by Maev et al. [74] as well as other research groups. However, the transmission acoustic microscopy poses some limitations such as the thickness of the specimen where it is placed between the two acoustic lenses (one for emitting and another for receiving the ultrasound) and some technical difficulties compared to the reflection mode [75]. Thus, the reflection scanning acoustic microscopy, where one acoustic lens has been utilized as a transmitter and a receiver, becomes accepted and widespread for its simplicity of operation, speedy and capability of resolving acoustic images.

2.2.1 Biological Applications and Tissue Characterization

The basic design of scanning acoustic microscope remains the same for years, while its practical realization has been improved in a wide variety of devices produced by commercial companies and developed in research laboratories. They are mainly used in two areas: industrial quality control and for biomedical applications [76]–[79]. The use of acoustic microscopy in medicine and biology has three main advantages. First, it can visualize with high-resolution tissues and cells in natural condition without the need for staining and fixation process. Second, it can successfully characterize micromechanical properties of biological objects by measuring the acoustic properties such as speed of sound, attenuation, and backscattering coefficient. Third, intensity images and echographic images were analogous for clinical ultrasound imaging study.

Since many physiological changes in tissues during diseases result in the modification in its characteristics, including elastic properties, detecting variations in these properties can provide insight into tissue's physiological state. Therefore, an acoustic microscope could be a powerful tool for differential medical diagnosis of diverse types of cancer. Liver carcinoma, gastric cancer, lesions of lymph nodes, breast and renal cancer were actively investigated by many research and groups [72], [77], [78], [80], [81]. It was discovered that tumour tissues exhibit distinct velocity and attenuation values comparing to healthy tissues, in spite of that the magnitude and indication of these pathological modification change for a various tumour. While cancer cells themselves show a decrease in sound speed and attenuation, the averaged values of these parameters for a tumour can be higher than the surrounding healthy tissue. This effect can be explained by the dynamic inclusion of stroma in the process of neoplasm growth [82]–[85]. Moreover, at a frequency

approximately higher than 300 MHz, individual cells can be resolved while at a frequency ranging from 1-1.5 GHz detailed information about their internal structure becomes apparent [83], [85], [74]. Many research groups has used acoustic microscopy for the observation of living or cultured cells in order to measure mechanical properties of the cells and derived elastic parameters of subcellular structures (Hela cell, leukemia, glial and glioma cells and others) [43], [74], [86], [87]. For instance, it was found that cancer cells (glioma cells) are less stiff than glial (normal cells) and that is related to less existence of cytoskeleton material around the nucleus in the tumour cells [87]. This result is proved by other studies on breast cancer cells that indicates low acoustic impedance and therefore lower stiffness than healthy cells [83].

Human skin is the largest organ that carries significant biomechanical functions and has a complex microstructure. The acoustic microscopy was used to investigate normal, melanoma skin cancer, wounded skin , inflammatory processes, regenerated skin, burn scars, and photodamaged skin [79], [88]–[92]. In-vivo studies of human skin done by Hozumi et al. using 100 and 120 MHz transducers, show the ability of acoustic microscopy to visualize microvessels, hair follicles and sebaceous glands at up to 1.2 mm depth.as echo poor density area in the 3D model. Skin morphology with all layers was also clearly visualized by this system. This 3D method is more advantageous than OCT and 20 MHz US. OCT cannot go deeper than approximately 600 μm in the skin and 20 MHz cannot visualize fine structures (hair follicles, microvessels, and sebaceous glands), respectively [93]–[95].

An ex-vivo study using SAM with 600 MHz demonstrates the ability to see individual cells in various inflammatory and cutaneous neoplasms. It was hard to define nuclear details

especially determining components of the inflammatory cell, and therefore early stage of the lesion cannot be identified. In this study, the diagnosis was limited with acoustic images without quantifying acoustic properties of individual cells that are related to its visco-elastic behaviour and thus SAM was not able to provide a definite diagnosis [96]. A recent study at 400 MHz has studied thin melanoma and differentiate between abnormal and normal based on tissue morphology and measured values of ultrasound velocities. In the same study, thick melanoma was evaluated by 50 MHz transducer and shows very high attenuation comparing to healthy tissue.

To the best of our knowledge, very few quantitative studies have reported ultrasonic imaging of different types of skin cancer (BCC, SCC, and melanoma) at ultra- high frequency (>300 MHz) measuring acoustic properties of individual cells, and therefore evaluating its elastic behaviour. Also, no study has been done before that calculates the acoustic impedance of melanoma skin cancer compared to normal.

CHAPTER 3

SCANNING ACOUSTIC MICROSCOPE

3.1 Imaging Principle

An overall review of acoustic microscopy principle is given in Brigg's book [97]. Here, we briefly describe the imaging technique that will be utilized in the present study. The operation of Honda SAM is based on a pulse-echo mode where the same transducer is used for transmission and reception of ultrasonic waves. This setup allows accomplishing frequency-domain analysis of the pulse resulting in a quantitative measurement or characterization of the reflection by power spectrum analysis.

An ultrasonic pulse wave is produced by the vibration of a piezoelectric transducer and transmitted to biological tissues through a coupling medium, i.e. deionized water. Biological tissues have an acoustic impedance close to that of water, and practically no contrast caused by the mismatch in reflection coefficient are displayed. Primarily, the contrast in the acoustic images is produced from the difference in attenuation across the tissues. For that reason, it is essential for the sample to be mounted onto substrates composed of highly reflective materials. The emitted sound wave is focused on a specific region of the target and is reflected from the interface between the substrate and the target. The focusing procedure was performed by moving the acoustic lens along its Z-axis towards the sample. The maximum amplitude of the reflected signal obtained during this motion means that reflecting surface is located precisely at the focal distance. The reflected ultrasonic beam is returned to the transducer and is converted into an electric signal. To form an acoustic image, the amplitude of the signal in specific time interval indicated by

the gate system is registered and represented as the brightness of the corresponding pixel. The scanning along sample surface (X- and Y- axis) allows to sequentially pass all pixels within square scanning area and to create corresponding two dimensional image (C-scan).
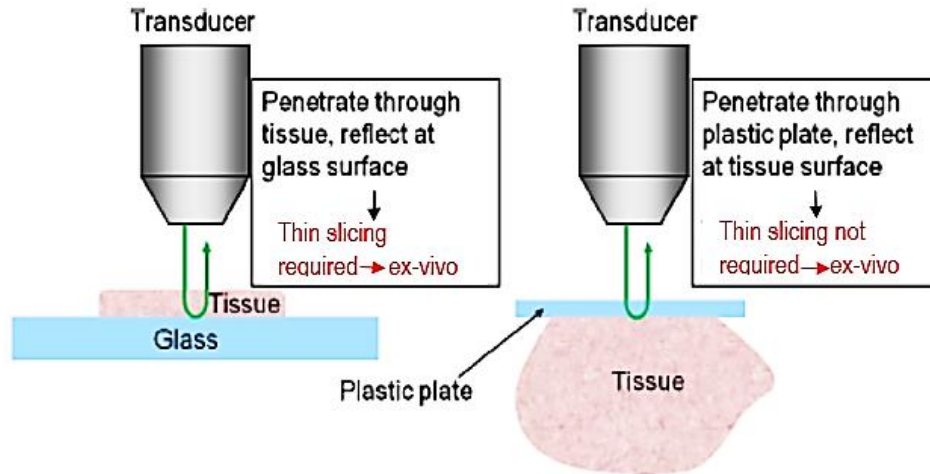
Figure 3.1: Schematic illustration of two modes of the scanning acoustic microscope. Left: sound speed mode, right: acoustic impedance mode [98].

The Honda microscope can operate in two modes of visualization: sound speed and acoustic impedance. The imaging mechanisms for both modes will be described underneath.

Figure 3.1 shows the schematic illustration of the beam propagation in the tissue for these operation modes. The left drawing displays the speed of sound mode used for accurate imaging when an ultrasonic wave propagates through the thinly sliced specimen (approximately about 10 μm of thickness) that is in direct contact with the transducer through the coupling medium. The ultrasonic wave reflects back at the interface between the sample and the glass. The right figure illustrates the impedance mode where the specimen is covered by the thin plastic plate, and the beam reflected from the plastic/tissue interface is analyzed. In this mode, the specimen doesn't require thin slicing or any other

special preparation. The positioning of the substrate (plastic plate) between the transducer and the sample prevents contamination of the equipment. This is a significant advantage allowing to examine fresh or fresh-frozen tissues.

3.2 General Description of Acoustic Lens

The acoustical lens that emits and focus the sound wave is vital element of the acoustic microscope. Focusing diminishes the lateral dimension of the beam in the focal point which dramatically improves lateral resolution. Accordingly, the intensity will be higher at the focal zone, and the signal to noise ratio will increase as well [99].

3.2.1 Design of the Transducer

The core of acoustic lens is a piezoelement-layer of material exhibit change in the thickness in response for the applied electrical field. It converts the electrical signal into pressure waves and vice versa. Longitudinal waves are produced from the oscillations of the crystal. The most effective excitation happens at the resonant frequency (f) when its thickness δ is half the wavelength. Thus, f is given by this equation [99]:

$$f = \frac{c_T}{2\delta} \tag{1}$$

Where c_T is the sound speed of the crystal.

In a frequency range 30-100 MHz, the most convenient material for piezoelement is polyvinylidene fluoride (PVDF) - a soft plastic which is produced in the form of thin film and can be formed into necessary shape. Acoustical lens usually contains PVDF film on the surface of spherical cavity directly in contact with a coupling liquid (Figure 3.2 A). The backing material, in this case, should have high attenuation in order to absorb all the reflection inside. Focal distance here equal to the radius of the spherical cavity.

For higher frequencies (above 100 MHz), the thickness of piesoelement becomes too small, and it is fabricated by vacuum deposition of piezoelectric material (usually ZnO) at the flat surface of hard buffer (fused quartz or sapphire). Sound wave is emitted into buffer volume, passes the buffer length and transmits into coupling liquid. The opposite surface of the buffer has a spherical cavity, creating a focusing lens (Figure 3.2 B) [100].
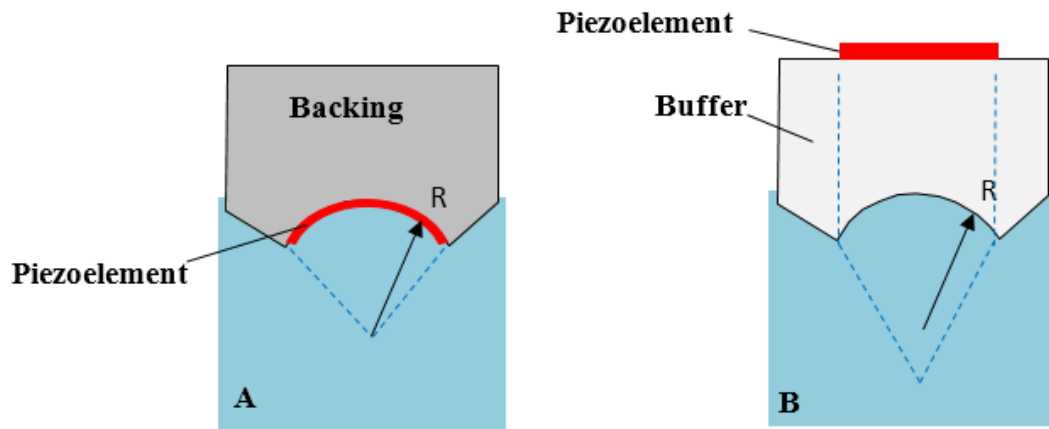
Figure 3.2: Design of PVDF transducer (A) and buffer rod transducer (B). R is the radius of curvature of the lens.

3.2.2 Beam Pattern for a Focused Transducer

The sound field of the transducer for focused and unfocused cases is presented in Figure 3.3. Theoretical description of this field is simplified for two regions which are Fresnel and Fraunhofer.
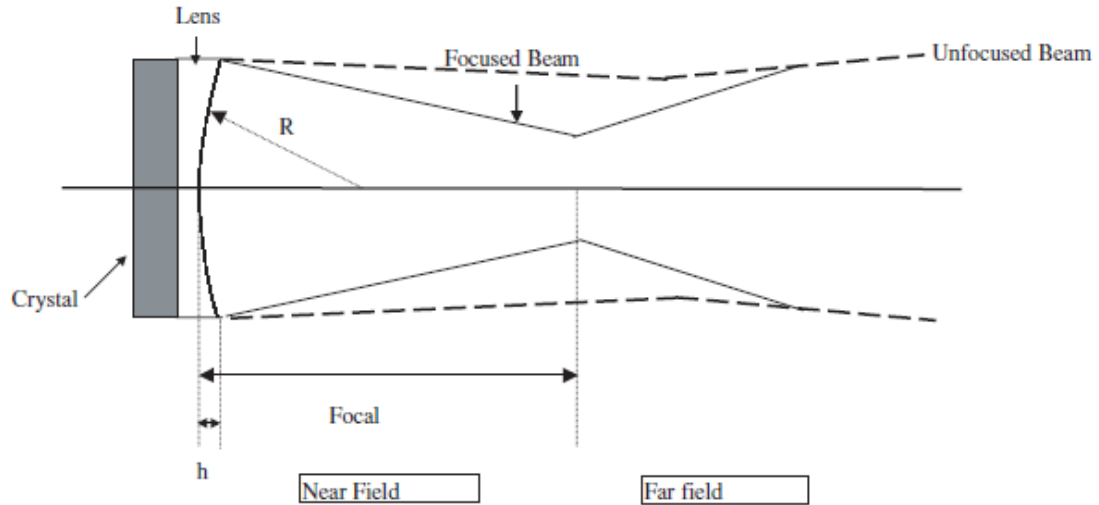
Figure 3.3: Schematic representation of the beam pattern formation for the transducer-lens system [99]. R is the radius of curvature of the lens surface, and h is the edge thickness of the lens.

The near-field is the region that comes up directly in front of the acoustic transducer. The length of the Fresnel region (N) is defined by the wavelength at certain frequency (f) in the medium and by the diameter aperture (D). The corresponding expression will be given by [99]:

$$N = \frac{D^2 f}{4\,c} = \frac{D^2}{4\lambda} \qquad (2)$$

For our particular high-frequency transducer 320 MHz with diameter 0.433mm we can estimate distance of near field equal 9.7 mm. As the focal distance for this transducer is 0.3 mm, we always working deep in near field area.

The Fraunhofer region is the area where the whole transducer can be considered as a point source. Here, the beam diverges, and the sound field pressure gradually decreases $\sim 1/z^2$ where z- distance from the transducer (Figure 3.4) [101].
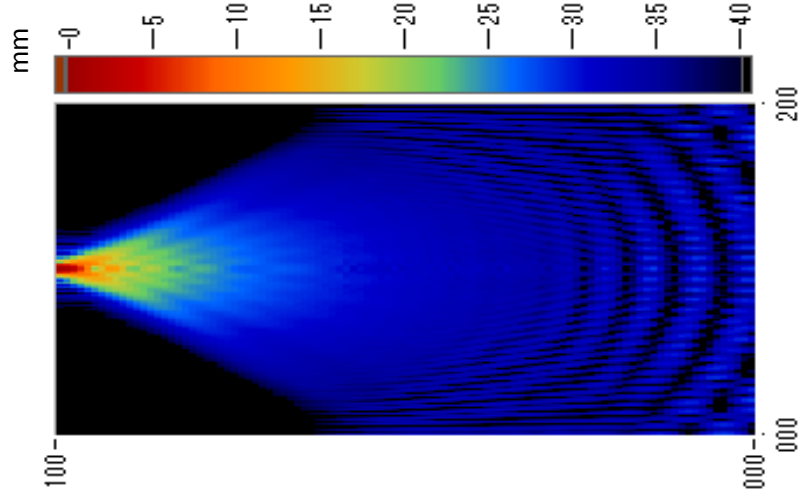
Figure 3.4: Reflection pattern in sound pressure.
Resolution- Along x: 1um/pt and along z: 2um/pt [thanks to Dr. Hozumi].

3.2.3. Resolution

The lateral resolution $\delta_{lateral}$ of the transducer is determined by the diameter of the focal

spot. This diameter is limited by diffraction phenomena and at level -3 dB this theoretical

limit equal:

$$\delta_{lateral} = 1.03\lambda \frac{f_0}{D} \tag{3}$$

Where $F = \frac{f_0}{D}$ is called F-number, characteristic of the lens.

The axial size of the focal point is referred as the depth of the field δ_{axial} and can be

calculated by the equation [101]:

$$\delta_{axial} = 4\lambda \frac{f_0^2}{D^2} \tag{4}$$

Where f_0 is the focal length of the lens.
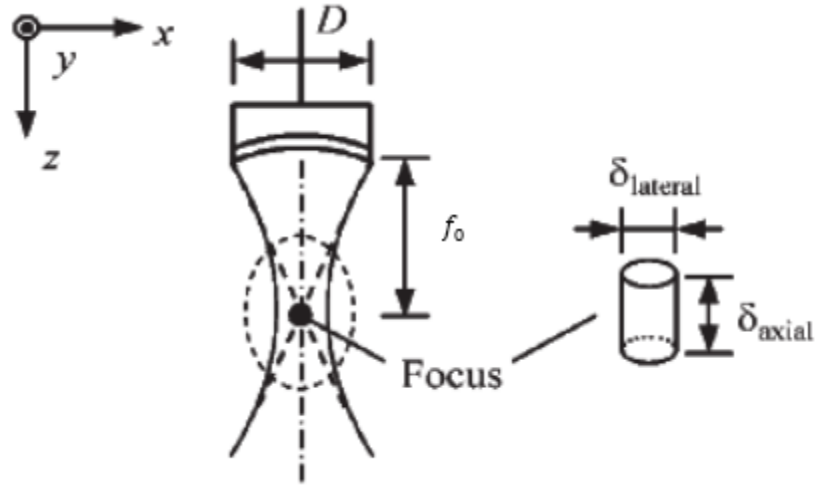
Figure 3.5: Resolution of the focused single element transducer [33].

3.3 Data Acquisition and Quantitative analysis

3.3.1 Speed of Sound Algorithm

In the speed of sound (SOS) mode AM 50SI acoustic microscope calculates the speed of sound in the thinly sliced sample. The pulses reflected from the front (S_s) and from the back (S_d) sides are overlapping as shown in Figure 3.6. This fact makes standard methods − measuring the time of flight- inapplicable [102]. The analysis of the interfered wave ($S_s + S_d$) by Fourier transform the time domain into frequency domain calculate the intensity and phase spectra that are normalized by the reference waveform (S_{ref}). In the frequency-domain analysis, the sound speed is calculated at the maximum and minimum frequency in the intensity spectrum. Thus, the thickness, attenuation and sound speed are calculated.
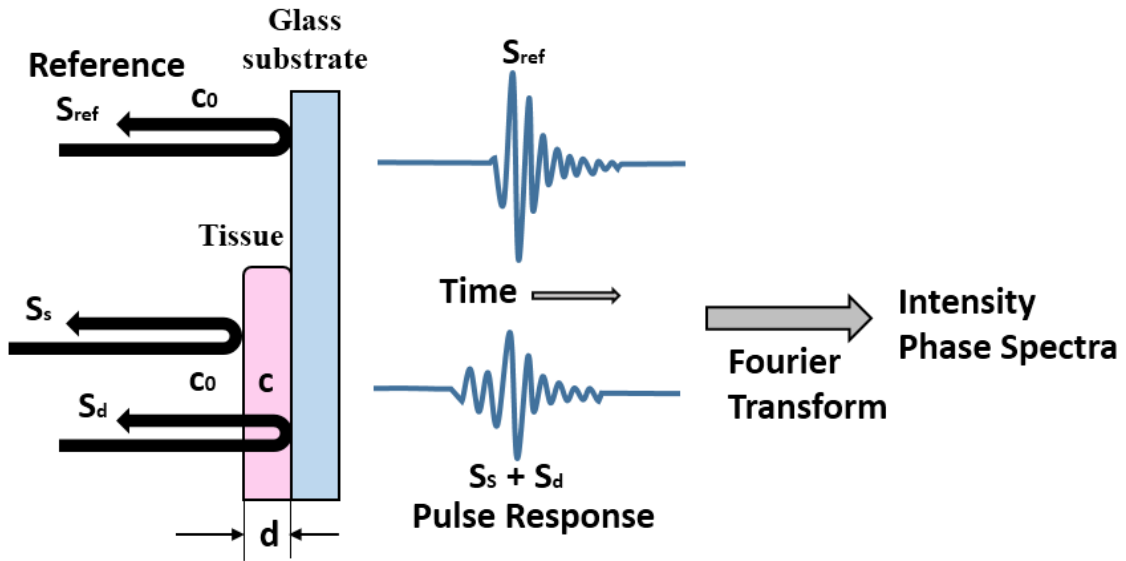
Figure 3.6: Illustration of the signal reflection in sound speed mode. *c_0, c and S_{ref} are the sound speed in water and tissue, and the reference signal respectively. S_s and S_d are the signals from the front and rear surface of the specimen, and d is the thickness of the specimen.*

3.3.1.1 Frequency Domain Analysis for Sound Speed
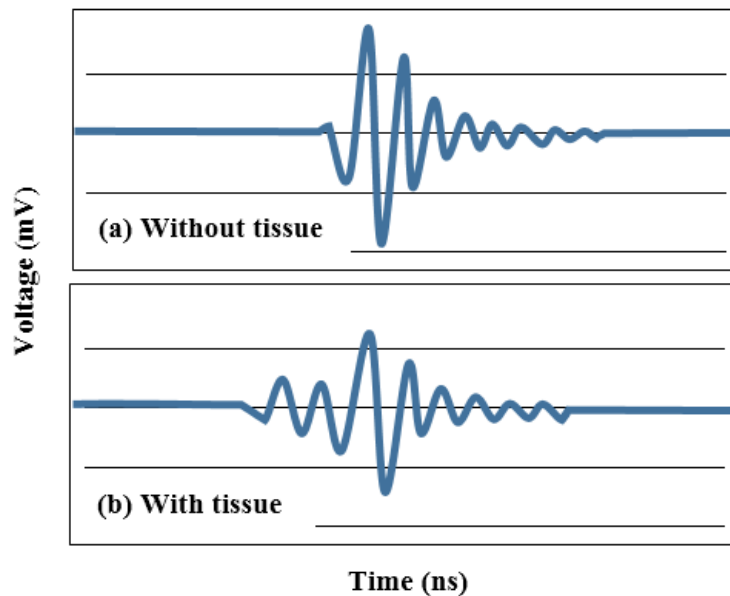
Figure 3.7: Illustration of waveforms from the glass substrate and specimen respectively in time - domain.

27

The example of the reflected waveforms is seen in Figure 3.7. Part (a) shows the reflection from the glass surface without the tissue. This signal was used as a reference waveform, and the point being defined as the reference point. Part (b) is the waveform from the tissue area that includes two components cannot be separated in time- domain. So, we can switch into frequency-domain and consider interference between the two reflections. Intensity and phase spectra were calculated by Fourier Transform. The position of the maximum and minimum points at these diagrams are key parameters. However, they cannot be precisely determined without the normalization of the intensity and phase spectra by the reference signal as given in Figure 3.8.
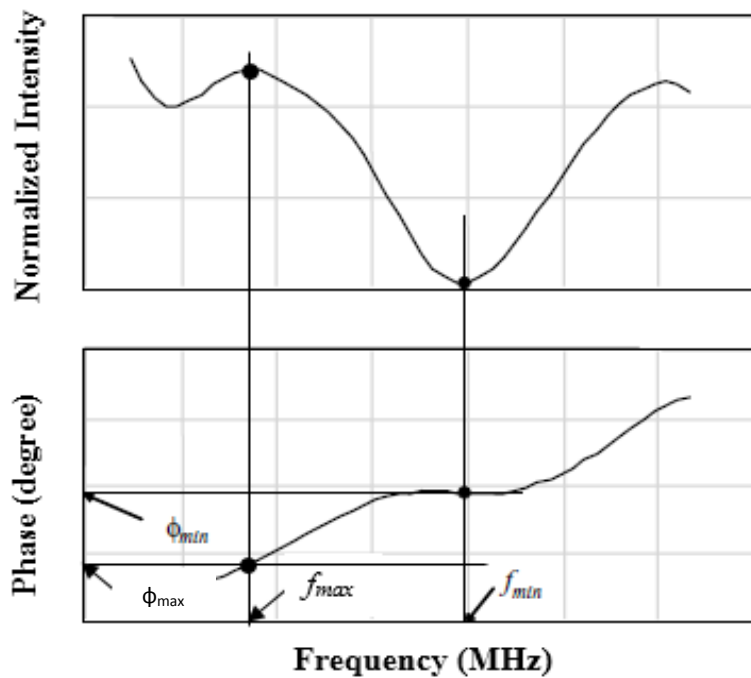
Figure 3.8: Frequency domain analysis of the interfered waveform [103].

28

The f_{min} is the minimum frequency in the normalized intensity spectrum with $\emptyset_{min}$ the corresponding phase angle as expressed in the graph above. The phase difference between the two reflections at the minimum point is $(2n - 1)\pi$ that refers to a destructive interference yields to:

$$2\pi f_{min} \times \frac{2d}{c_0} = \emptyset_{min} + (2n - 1)\pi \tag{5}$$

Where d, c_0, and n are the tissue thickness, sound speed in water, and a non-negative integer, respectively.

Assuming now f_{max} is the maximum frequency in the intensity spectrum and $\emptyset_{max}$ as the corresponding phase angle, the phase difference at the maximum point is $2n\pi$ for a constructive interference giving:

$$2\pi f_{max} \times \frac{2d}{c_0} = \emptyset_{max} + 2n\pi \tag{6}$$

Then, the phase angles $\emptyset_{min}$ and $\emptyset_{max}$ can be expressed as follows by:

$$2\pi f_{min} \times 2d \left(\frac{1}{c_0} - \frac{1}{c}\right) = \emptyset_{min} \tag{7}$$

$$2\pi f_{max} \times 2d \left(\frac{1}{c_0} - \frac{1}{c}\right) = \emptyset_{max} \tag{8}$$

Where c is the speed of sound in the sample.

Since $\emptyset_{min}$ and $\emptyset_{max}$ is the phase difference between the wave that passed a distance 2d in the tissue with a sound speed c and the wave that passed in water through the corresponding distance with sound speed c_0. By solving the simultaneous equations of (5) and (7), the thickness value at the minimum point is given by:

$$d = \frac{c_0}{4\pi f_{min}} \{\emptyset_{min} + (2n - 1)\pi\} \tag{9}$$

Then, the sound velocity will be calculated as:

$$c = \left(\frac{1}{c_0} - \frac{\emptyset_{min}}{4\pi f_{min}d}\right)^{-1} \tag{10}$$

For the maximum point, by resolving (6) and (8) yields to:

$$d = \frac{c_0}{4\pi f_{max}}\{\emptyset_{max} + 2n\pi\} \tag{11}$$

Thence, the sound speed at this frequency will be given as [103]:

$$c = \left(\frac{1}{c_0} - \frac{\emptyset_{max}}{4\pi f_{max}d}\right)^{-1} \tag{12}$$

The slope of attenuation is subsequently obtained from the thickness (9) and the amplitude (15) equations at the minimum points as:

$$A = \frac{L}{f_{min}\, d} = \frac{L}{f_{min}} \left(\frac{c_0}{4\pi f_{min}}\{\emptyset_{min} + (2n - 1)\pi\}\right)^{-1} \tag{13}$$

And at the maximum points form equations (11) and (15), the slope of attenuation will be:

$$A = \frac{L}{f_{max}\, d} = \frac{L}{f_{max}} \left(\frac{c_0}{4\pi f_{max}}\{\emptyset_{max} + 2n\pi\}\right)^{-1} \tag{14}$$

Where

$$L = -10\, log\left(\frac{P}{P_0}\right)^2 \tag{15}$$

is the amplitude of the reflected wave [76]. P is the sound power of reflection from the tissue and P_0 is the sound power of reflection from the glass [104].

3.3.1.2 Viscosity and Elasticity Estimation

The longitudinal wave velocity resulting from the frequency-dependent characteristics of the amplitude and the phase of the received signals relates to the elastic modulus:

$$c = \sqrt{\frac{(K+4G/3)}{\rho}}$$ (16)

Where K is the elastic bulk modulus, G is the shear modulus, and ρ is the density of the sample.

In human tissues, shear modulus is much smaller comparing to the bulk modulus and therefore cam be neglected. Thus, the relation between the sound speed and the bulk modulus for the liquid-like material will be simplified in the form below:

$$c = \sqrt{\frac{K}{\rho}}$$ (17)

On the other hand, the tissue's bulk modulus K could be expressed in function of the elastic modulus E (Young's modulus) by:

$$K = \frac{(1+\sigma)(1-2\sigma)}{(1-\sigma)} E$$ (18)

Where σ is the material Poisson's ratio [105]. Poisson's ratio is considered to be equal approximately 0.5 in human soft tissues that corresponds to incompressibility condition [106].

Attenuation of sound is an important parameter that contributes to the contrast in an acoustic image. In the skin tissue, the viscosity is one of the main factors responsible for the attenuation of sound. For soft materials, the viscosity is given by the absorption coefficient as:

$$\alpha = \frac{2f^2\pi^2}{3\rho c^2}\left(\eta_v + \frac{4}{3}\eta_s\right)$$ (19)

Where η_v is the volumetric viscosity and η_s is the shear viscosity [98].

3.3.2 Acoustic Impedance Algorithm

The acoustic impedance (AI) was calculated for the thickly cut skin specimens examined in the acoustic impedance mode. For acoustic impedance determination, vertical incidence analysis of the returned waves from the target and the reference material was applied to obtain the acoustic intensity waveforms from a small angle of the focused transducer. These two reflections may be seen in the same field of view; however, if this is unrealistic, they may be observed independently under similar conditions, as shown in figure 3.9. The system is calibrated prior to the observation by a reference signal from the substrate material only without the tissue. The reflections from the reference substance (S_{ref}) and the tissue (S_{tgt}) were compared and explicated into the characteristic acoustic impedance (Z_{tgt}) by a numerical analysis of the sound field in the frequency domain using Fourier Transform was applied pursued by a calibration curve.
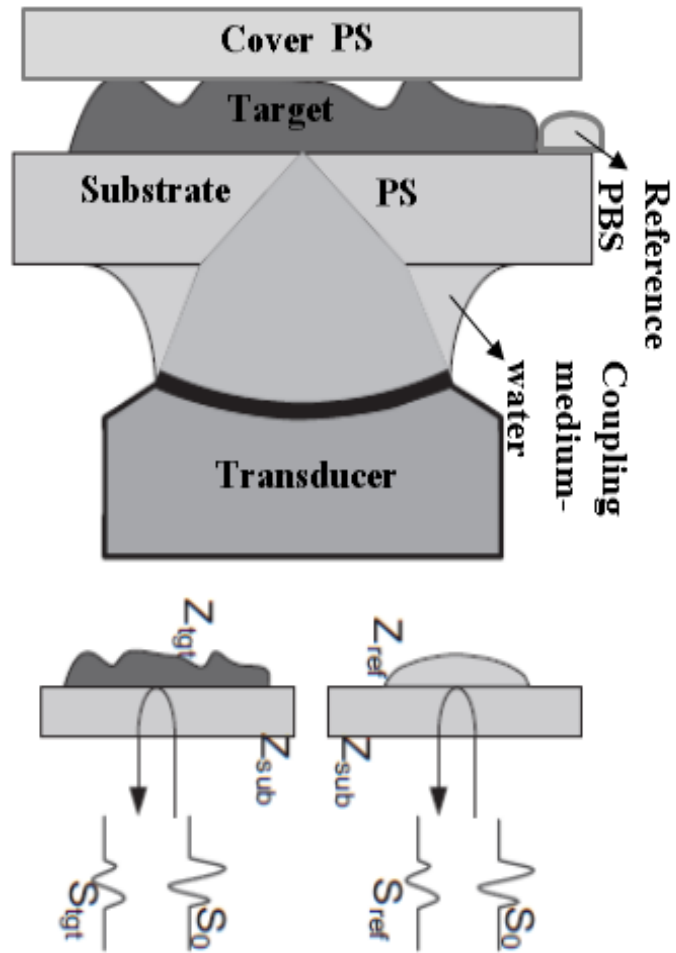
Figure 3.9: Representation of the signal reflection in AI mode assuming vertical incidence.

3.3.2.1 Frequency Domain Analysis for Acoustic Impedance
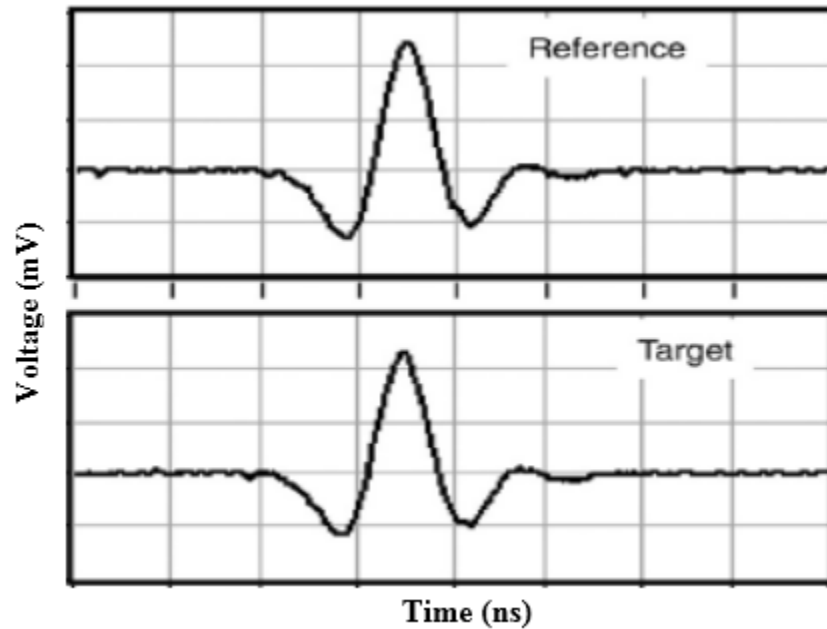
Figure 3.10: Illustration of reflected waveforms from the reference and the target respectively in time- domain [107].

The upper waveform on the Figure 3.10 shows the reflected response from the plastic substrate with phosphate buffer solution present and reflected waveform from the cross-section of the skin tissue in the time domain. The reflected waveform from the skin is very similar but slightly smaller to that reference waveform. One can conclude that skin tissue has the acoustic impedance similar to PBS solution. Frequency domain analysis of these two reflections was used to calculate acoustic impedance.
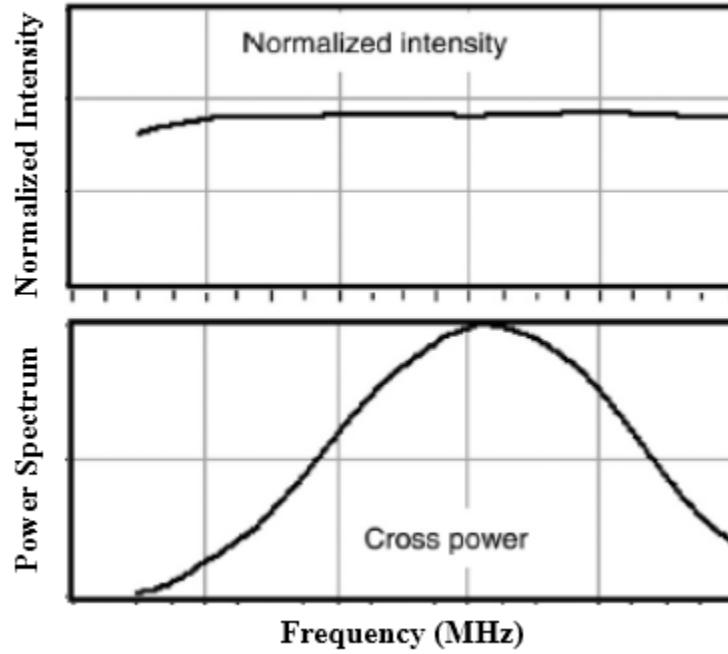
Figure 3.11: Frequency domain analysis of the target and reference signals [107].

Figure 3.11 displays the normalized intensity that represents the intensity of the target

signal by the reference signal and the cross-power spectrum calculated from the target and

the reference signals.

If the incident angle of the sound can be approximated as perpendicular to the target, the

intensity of the reflected wave can be described in function of the reflection coefficient as:

$$S_{ref} = \frac{Z_{ref} - Z_{sub}}{Z_{ref} + Z_{sub}} S_0 \tag{20}$$

And

$$S_{tgt} = \frac{Z_{tgt} - Z_{sub}}{Z_{tgt} + Z_{sub}} S_0 \tag{21}$$

Where S_0 is the transmitted sound, S_{tgt} and S_{ref} are the signals reflected from the target and

from the reference at an arbitrary frequency, respectively. Z_{tgt}, Z_{ref} and Z_{sub} are the acoustic

impedances of the target, reference, and substrate respectively [107]. Therefore, Z_{tgt} will be expressed from Eq. (21) as:

$$Z_{tgt} = \frac{1+\frac{S_{tgt}}{S_0}}{1-\frac{S_{tgt}}{S_0}} \, Z_{sub} \tag{22}$$

It is easy to measure S_{ref} and S_{tgt} but S_0 cannot be directly measured. Hence, by substituting Eq. (20) into Eq. (22) and assuming S_0 is constant all over the observation, the acoustic impedance of the target can be calculated as shown in Eq. (23):

$$Z_{tgt} = \frac{1-\frac{S_{tgt}}{S_{ref}}(\frac{Z_{sub}-Z_{ref}}{Z_{sub}+Z_{ref}})}{1+\frac{S_{tgt}}{S_{ref}}(\frac{Z_{sub}-Z_{ref}}{Z_{sub}+Z_{ref}})} \, Z_{sub} \tag{23}$$

Where $\frac{S_{tgt}}{S_{ref}}$ assumes fluid-fluid boundaries with normal incidence where no shear waves are taking into consideration [84].

3.3.2.2 Elasticity Estimation

The characteristic acoustic impedance is proportional to the speed of sound and the density of the tissue by this expression [98]:

$$Z_{tgt} = \rho c \tag{24}$$

As the target is soft tissue, its acoustic impedance in pressure wave is appreciably affected by bulk modulus that is estimated from the longitudinal sound speed in Eq. (17) and thus [108]:

$$K = \rho c^2 = \frac{Z_{tgt}^2}{\rho} \tag{25}$$

CHAPTER 4

MATERIALS AND METHODS

4.1 Honda Scanning Acoustic Microscope

The study was performed using specially designed for biological applications AMS-50SI scanning acoustic microscope (Honda Electronics, Toyohashi, Japan). It permits observation the morphology and measures biomechanical properties of biological objects in the frequency range 30-500 MHz. The microscope is equipped with the set of spherically focused broadband transducers with central frequencies 50, 120 and 320 MHz.
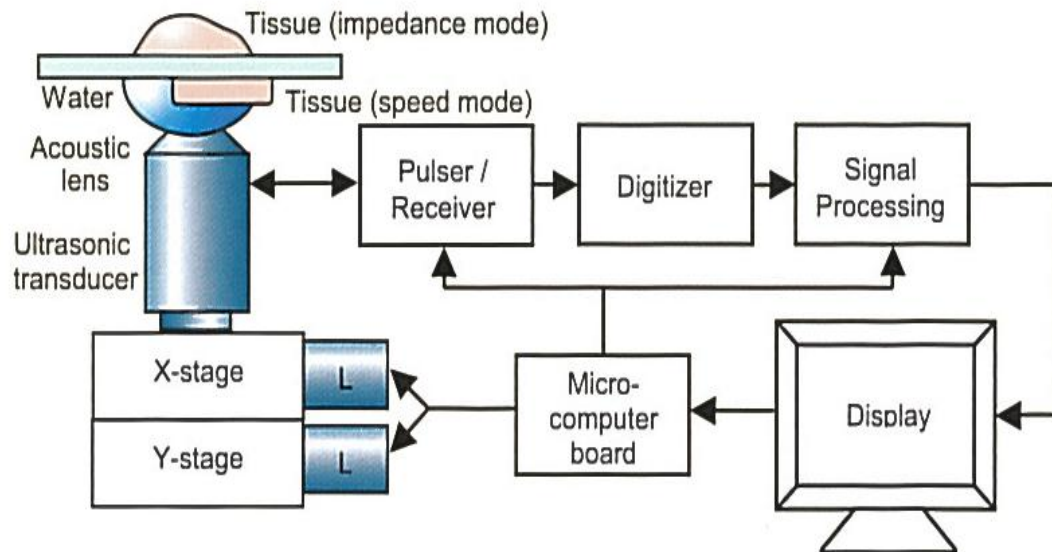
Figure 4.1: Block diagram of the biological acoustic microscope system, Honda Electronics Co. Ltd. [109].

Figure 4.1 shows a block diagram of the microscopy system. An electric impulse was generated by a pulse generator and applied to the piezoelectric element of the transducer. The transducer converts the electrical radiofrequency signal to a short ultrasonic pulse wave, which was then focused by a spherical lens and propagate through coupling liquid toward the substrate where histology specimens are mounted. The pulse width of about 0.5 ns, the pulse voltage of 40 V, and the pulse repetition time around 4 μs was emitted and received by the same transducer above the specimen. The reflected from the tissue signals after corresponding amplification were introduced into 2GS/s digitizer board installed in the Windows-based PC. To reduce random noise, eight pulse echo sequences with 200 sampling points were averaged for each scan. The transducer was mounted on an X-Y stage with linear stepper motors that were driven by the controller in order to provide its motion according to the scanning pattern. All the components of the acoustic microscope are controlled by specialized software with user-friendly interface. We can choose the scanning area to be 0.6 mm × 0.6 mm, 1.2 mm × 1.2 mm, 2.4 mm × 2.4 mm, or 4.8 mm × 4.8 mm and the size of C-scan up to 500×500 pixels. The time of scanning depends on the number of scan points. In the present study, we scanned the histological slide at 500×500 points in the 2.4 mm × 2.4 mm area and below. The total scanning time required was about 2 to 3 min. Two-dimensional profiles of reflection intensity and created colour-coded images were obtained for sound speed and acoustic impedance modes. All the measurements for both modes were performed at room temperature.

4.2 High-Frequency Imaging Experimental Setup

For speed of sound mode, thinly skin tissues were imaged with an acoustic lens operating at a frequency of 320 MHz. An ultrasonic pulse wave is produced by the vibration of a piezoelectric transducer (ZnO) located on the top of a long buffer rod made of a single crystal of sapphire. It travels later to a spherical lens located at the bottom of the buffer rod. The lens converts the ultrasonic plane wave to an ultrasonic spherical wave. The slide section is placed upside-down on the stage above the transducer. A small drop of distilled water was applied as a coupling medium between the transducer and the sample. The skin specimen is placed on a glass substrate. The emitted sound wave is focused on a specific region of the target and is reflected at the front and rear side of the sliced tissue. The reflected ultrasonic beam is returned to the transducer and is converted into an electric signal. When the scanning is completed, C-scan along with additional images, representing the two-dimensional distribution of calculated parameters (sound speed, attenuation, and thickness) are obtained.

The images are provided with dimensional rulers and pseudo-color bar scale. The range of values varies from 1350-2000 m/s for sound speed and from 0-15 dB/mm for attenuation. The region of interest (ROI) on the acoustic images was determined from the optical microscopic observations to point out histopathological features that differentiate between the lesion and non-lesion areas. For each sample, the sound speed and the attenuation constant were acquired from the average of 50 pixels values in the ROI in the lesion area and the healthy skin part away from the abnormal area. The results for all the specimens are given as mean values ± 1SD. However, the step for the determination of thickness could

involve 5% error, so the attenuation and speed of sound values had 5% error. As the range for the velocity of sound was between 1350-2000 m/s, so the error would be about 100 m/s.

4.2.1 320 MHz Transducer

An ultrasonic wave is typically attenuated in proportion to the square of its frequency. For high frequency, the ultrasonic wave cannot penetrate deep enough into the human tissue. However, at the lower frequency, the ultrasound can propagate deeper without loss of the wave amplitude but with relatively limited resolution. In my particular case, my study was specified to resolve individual cells on the surface. For that reason, most of research was performed with 320 MHz acoustic lens, which has a buffer rod design. The piezoelectric layer of ZnO with crystallographic orientation corresponding to Z-cut is placed on the plane surface of a long sapphire buffer rod with a spherical cavity ground at the base as shown in Figure 4.2. The sound velocity of ZnO is equal to $c_T = 6330$ m/s [110]. The center of curvature of the point-focused lens marked at point C and the focal point at F along Z-axis. The focal distance f_0 of the acoustic lens could be calculated by the relation with an analogy to optical lenses:

$$f_0 = \frac{R}{\left(1 - {v_c}/{v_s}\right)} \tag{26}$$

Where v_c is the sound velocity of the coupling medium (water), v_s is the acoustic velocity in the buffer rod, and R is the curvature radius [110].
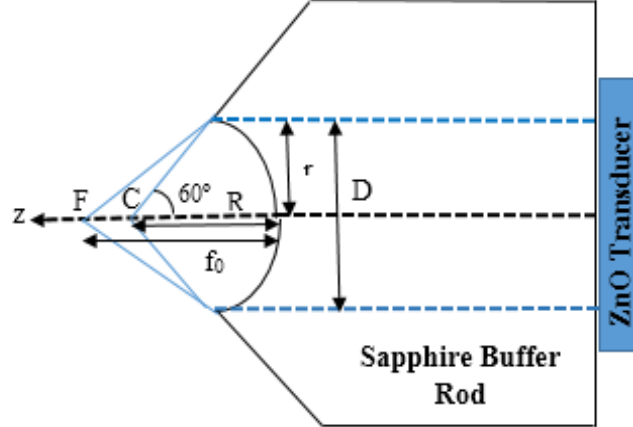
Figure 4.2: Detailed diagram of the 320 MHz transducer.

The refractive index, $\bar{c} = \frac{v_c}{v_s}$ is less than 1. The smaller the index of refraction the smaller

is the angle of refraction towards the center of curvature of the lens and therefore the

spherical aberrations at the focal point are small [111]. Also, it is stated that concave lens

uses less substance than a convex lens and thus acoustic aberration is minimal [112].

The entrance pupil of the lens (D) is specified by the diameter of the circle at the extreme

edge of the sapphire lens and is computed from this equation:

$$\sin \theta = \frac{D}{2\,R} \tag{28}$$

With θ is the half aperture angle.

The detailed characteristics of the 320 MHz lens will be simplified in this given Table.

It is important to notice that the lateral resolution has to be at least the same size of the cell

for cellular resolution imaging. As shown below in Table 4.2, it is about 3.2 μm sufficient

for cell visualization in the tissue.

Table 4.1: Characteristics of the sapphire lens at 320 MHz.

Characteristics of the Lens	Values
Half aperture angle	60°
Geometric radius	0.25 mm
Sapphire lens radius	0.2165 mm
Sound speed of sapphire	11180 m/s
Sound speed of water	1485 m/s
Focal length	0.288 mm
Aperture diameter	0.433mm
Axial Resolution	8.21 µm
Lateral Resolution	3.2 µm

4.2.2 Histological Thin Skin Samples

Healthy and abnormal skin samples used in this study were provided by Windsor Regional Hospital (WRH). The research protocol was approved by the Research Ethics Board (REB) at the University of Windsor and the Windsor Regional Hospital. Different types of skin cancer were selected: Basal Cell carcinoma (BCC), Squamous Cell Carcinoma (SCC), Melanoma. Those tissues were fixed in 10% formalin, embedded in paraffin, cut to a thickness of 5~8 µm with a microtome and affixed to a glass substrate without being covered by a coverslip. For ultrasonic examination, the specimens need to be deparaffinized without the necessity of staining. This deparaffinization process (Table 4.1) includes immersion in the series of prepared chemical solutions of xylene and ethanol with

different concentrations to remove the paraffin wax and rehydrate tissue. After, the slides are placed in a running water bath to rinse off ethanol. As deparaffinized samples dry up very quickly, they were stored at +4°C in tightly closed slide holder, covered by a wet piece of cotton and deposit in a cool, moist environment to extend their usage life.

The immersion in Xylene during deparaffinization causes the dissolving and elution of most fat from the skin samples as shown in Figure 4.2. However, in our case, the measurement of acoustic properties was restricted in the epidermis and dermis layer only. The adjacent slide sample was stained with Hematoxylin and Eosin (H&E) for optical microscopy.

Table 4.2: Deparaffinization protocol [88].

Solutions bath (concentration)	Incubation time
Xylene 99%	5-10 min
Xylene 99%	5 min
Ethanol 95%	1-3 min
Ethanol 95%	3 min
Ethanol 80%	3 min
Ethanol 70%	3 min
Distilled water	1-3 min
Distilled water	3 min

Figure 4.3: Histological skin samples, paraffinized (left) and deparaffinized (right).

4.3 Low-Frequency Imaging Experimental Setup

In the acoustic impedance mode, the device can image the local distribution of characteristic acoustic impedance of the tissue. For the most of our measurements in this mode, the PVDF transducer with a centre frequency 50 MHz was used. The ultrasonic beam was focused on the plastic/tissue interface. The gate system was adjusted on the reflection pulse from this interface. After precise levelling the experimental stage, a two-dimensional scanning was performed to obtain the characteristic acoustic impedance image.

The values of the acoustic impedance in human tissue vary from 1.5 to 2 N.s/m^3. The measurement of the characteristic acoustic impedance was done in the ROI for each tissue sample by the mean of 20 pixels values with the standard deviation. When regions with PBS or air were present in the image due to the specimen roughness, they were excluded from the measurements.
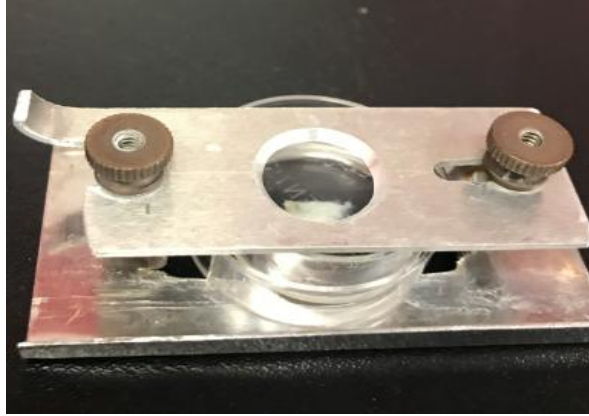
Figure 4.4: Holder chamber used for a fixed tissue for acoustic impedance imaging.

The sample is placed in the chamber, formed by the bottom of standard 1.5" Nunc Petri dish and the 0.83 mm thick polystyrene substrate squeezed together in the holder (Figure 4.4). The drop of distilled water (Z_w= 1.49 MRayl) was used as a coupling between the substrate and the transducer. The substrate material- polystyrene with Z_{sub}=2.46 MRayl [113] provides a compromise between the transmitted and reflected signal at the interface and has low sound attenuation. Phosphate buffer solution (PBS, 5%) was used as a coupling liquid between the specimen and the plastic plate. The PBS solution was also used as a reference in the calculation of acoustic impedance values of the skin, its AI value (Z_{ref}=1.54 MRayl) [83] is close to the human skin.

4.3.1 50 MHz Transducer

Thickly sectioned tissues were imaged with an acoustic lens operating at a frequency of 50 MHz that allows to form image of the internal focal plane of the specimen but with low resolution. It provides a lateral resolution of 40 μm where it is impossible to recognize skin cells on the obtained images. However, this study was done for calibration for in-vivo acoustic impedance measurement in the long term goal and the choice of 50 MHz is a

reasonable frequency to create a good compromise between resolution and penetration depth. The characteristics of the 50 MHz lens are given in Table 4.3.

Table 4.3: Characteristics of 50 MHz Transducer.

Characteristics of the Lens	Values
Half aperture angle	22º
Focal length	3.2 mm
Aperture diameter	2.4 mm
Axial Resolution	211 µm
Lateral Resolution	41 µm

4.3.2 Thickly Sliced Skin

WRH provided the 2×2 cm skin specimens of healthy skin and melanoma lesions, fixed in 10% formalin (Figure 4.5). In the abnormal tissue, a dark brown portion indicates melanoma tumour area and that differs from healthy skin. The hypodermis layer (fatty layer) was cut by a razor blade and removed to ease further sample preparation. This ultrasonic visualization method doesn't require thin slicing of the biological tissue. The skin tissue needs only to be immersed in phosphate buffered saline (PBS), a water-based salt solution, and placed on a transparent plastic substrate before the imaging. The slices with a thickness of 500 µm were prepared with the razor blade. When the samples are not being used for experimental scanning, they were stored in 10% formalin and +4°C to keep them away from drying.
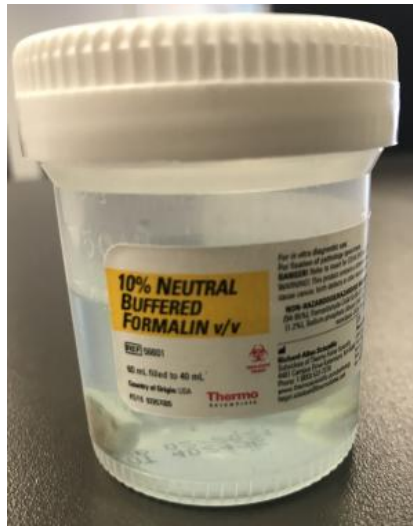
Figure 4.5: Formalin fixed thick skin tissue.

CHAPTER 5

EXPERIMENTAL RESULTS AND DISCUSSION

5.1 Evaluation of Speed of Sound and Attenuation of Skin Histological Slices

Quantitative ultrasonic study of skin specimens was performed to identify morphology and diagnostic features for healthy skin and different types of cutaneous cancer that being confirmed later by a pathologist. Acoustic skin images obtained by SAM were compared to optical H&E stained images. For all samples, acoustic properties measurements for the chosen healthy regions away from the pathological areas were also acquired as reference data to distinguish between healthy and cancerous tissues. The data were represented as mean values ± SD.

5.1.1 Healthy Skin

Healthy skin properties were determined from region positioned away from the tumour area in diseased tissue which means on the leftmost and rightmost part of the specimen.

Figure 5.1 shows the typical acoustic image of the healthy skin with its corresponding H&E light microscopy. The two primary layers of the human skin were clearly identifiable on both acoustic and optical images. The thin epidermis (E) layer is seen as a light gray colour line on the acoustic intensity image and as a dark violet stained in the optical one. The thick dermis (D), beneath the epidermis, is comprised of two layers subsequently that are detectable on both images: the papillary dermis (PD) and the reticular dermis (RD). The papillary dermis indicated by a rectangle is made of separated connective tissue like a loose

mesh [88]. The thicker reticular dermis below has denser, irregular connective tissue with dense collagen and elastin fibres.
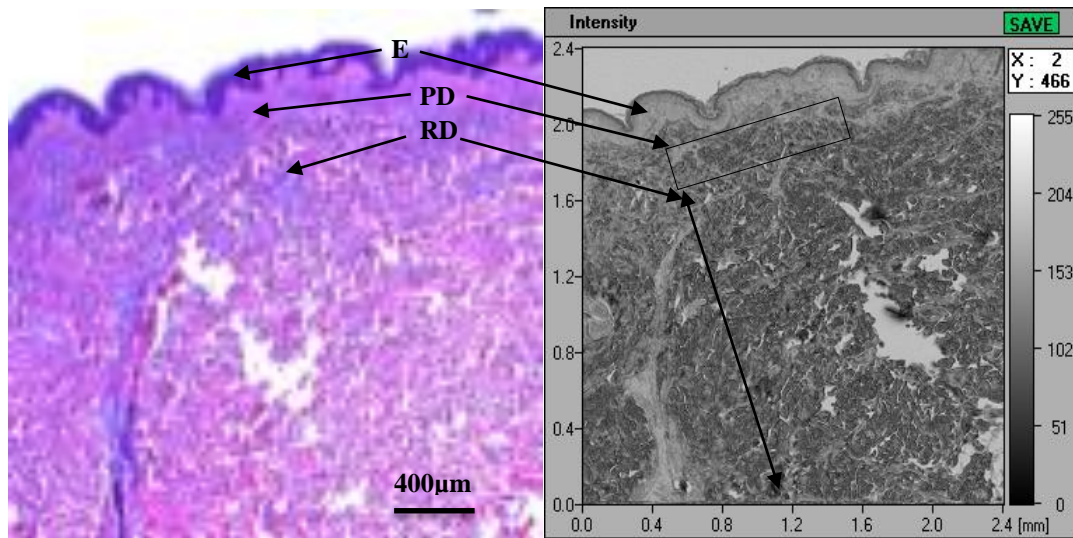
Figure 5.1: The acoustic image of healthy skin tissue (right) and its corresponding light microscopic image with H&E staining (left). *E: epidermis, PD: papillary dermis, RD: reticular dermis. The black rectangle indicates papillary dermis region.*

As shown in Figure 5.2, all layers have the distinct speed of sound and attenuation values. The thicker reticular layer is marked with the highest speed of sound (1800 ±50 m/s) and attenuation (12.8 ±0.6 dB/mm); this agrees with the presence of a significant number of dense collagen fibres in this skin part.
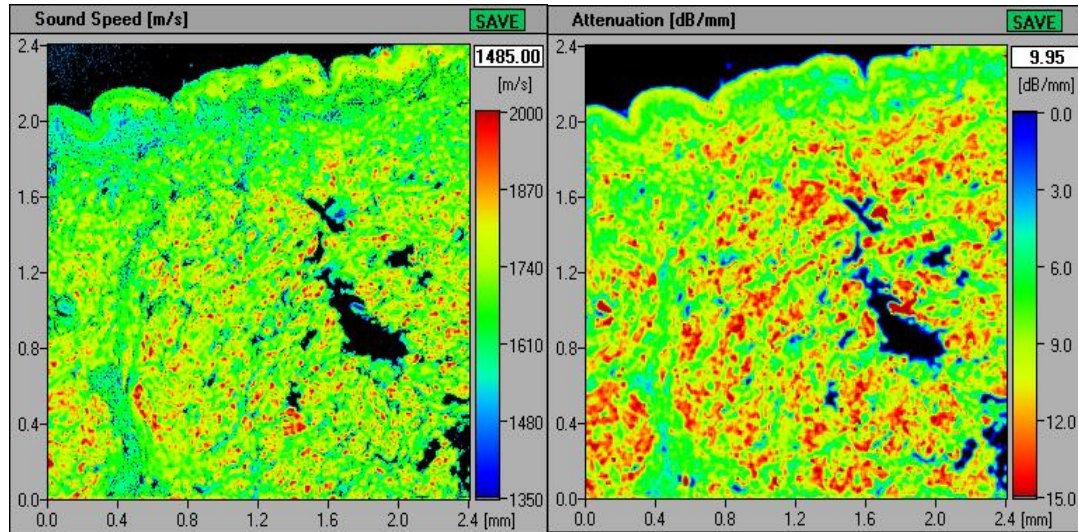
Figure 5.2: Images of sound speed (SOS) and attenuation of sound (AOS) in healthy skin referred to the Figure 5.1.
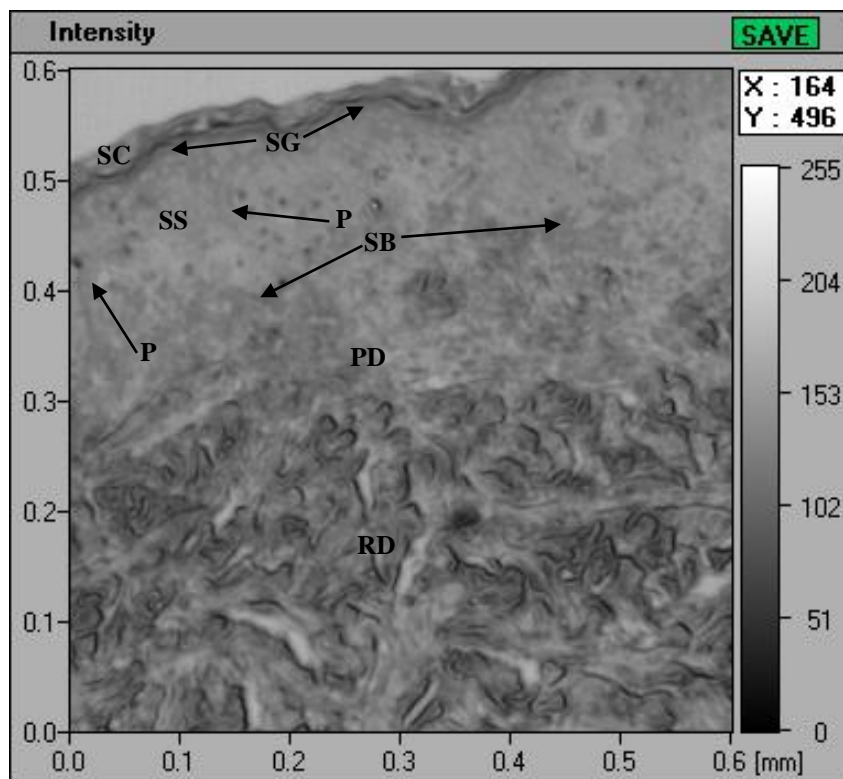
Figure 5.3: Acoustic intensity image of healthy skin with a scan area of 0.6×0.6 mm^2 by 500×500 pixels. *SC: stratum corneum, SG: stratum granulosum, SS: stratum spinosum, SB: stratum basale, P: papillae.*

Higher magnification provides more details of skin structure as seen in Figure 5.3. Individual cells can be easily detected. We can efficiently discriminate among all fine structures in the epidermis layer. The well-demarcated line at the top of the epidermis corresponds to the stratum corneum, a keratin layer with high sound attenuation. The cornified outer layer (SC) followed by the stratum garnulosum (SG), stratum spinosum (SS), and the basal layer (SB) that adjoins the papillary dermis. At the epidermal/dermal junction, some dermal papillae (P) are visible like downwards folds of the epidermis. Also, in reticular dermis (RD), connective tissues are well- delaminated.

The averaged values for the speed of sound and the attenuation are illustrated in Table 5.1.

Table 5.1: Average SOS and AOS for main layers of healthy skin.

Skin Layer	Average SOS (m/s)	Average AOS (dB/mm)
Epidermis	1700 ±20	9.0 ±0.5
Papillary Dermis	1660 ±30	10.0 ±0.6
Reticular Dermis	1800 ±50	12.8 ±0.6

5.1.2 Squamous Cell Carcinoma

A-well differentiated squamous cell carcinoma (SCC) is shown in Figure 5.4. It is an invasive type of cutaneous cancer at the advanced stage since the tumour invades very deep into the dermis and reaches the hypodermis layer. The basement membrane is destroyed; also it is hard to specify the location of the epidermis and the two sub-layers of the dermis. Several large irregular tumour cell clusters (AC) are spread all over the dermis that is considered as a typical feature for carcinoma [85]. These clusters are discerned by light

gray to white colour in the acoustic image. In the optical image, those features are stained preferably with Hematoxylin which stains the cell nuclei with the violet or blue as shown in Figure 5.5. Those cancer nests will be transformed later into keratinized squames and will form ring-shaped nodules with concentric, laminated layers, called keratinous pearls (KP) indicated by dark gray areas in the acoustic image and as pink (abundant eosinophilic) on the optical image, respectively. The outer contours of the SCC lesion are non-uniform due to the excessive keratinization.
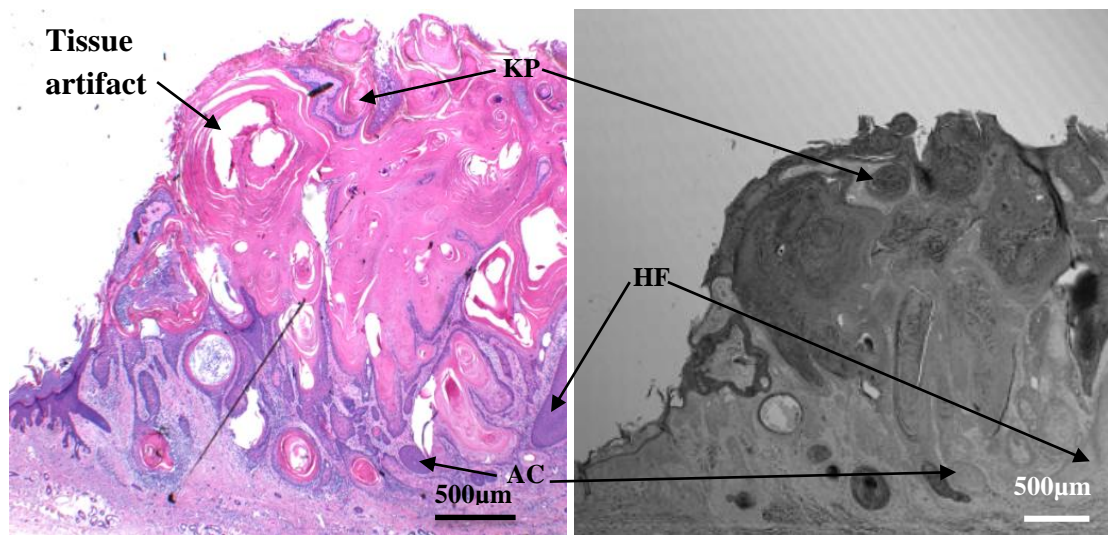
Figure 5.4: Comparison of acoustic image of well- differentiated squamous cell carcinoma (right) with its corresponding H&E image (left). *KP: keratinous pearls, AC: abnormal squamous cells cluster, HF: Hair follicle.*
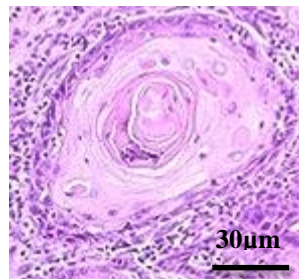
Figure 5.5: Abnormal squamous cells cluster (AC) with keratin formation at higher magnification (H &E staining).

52
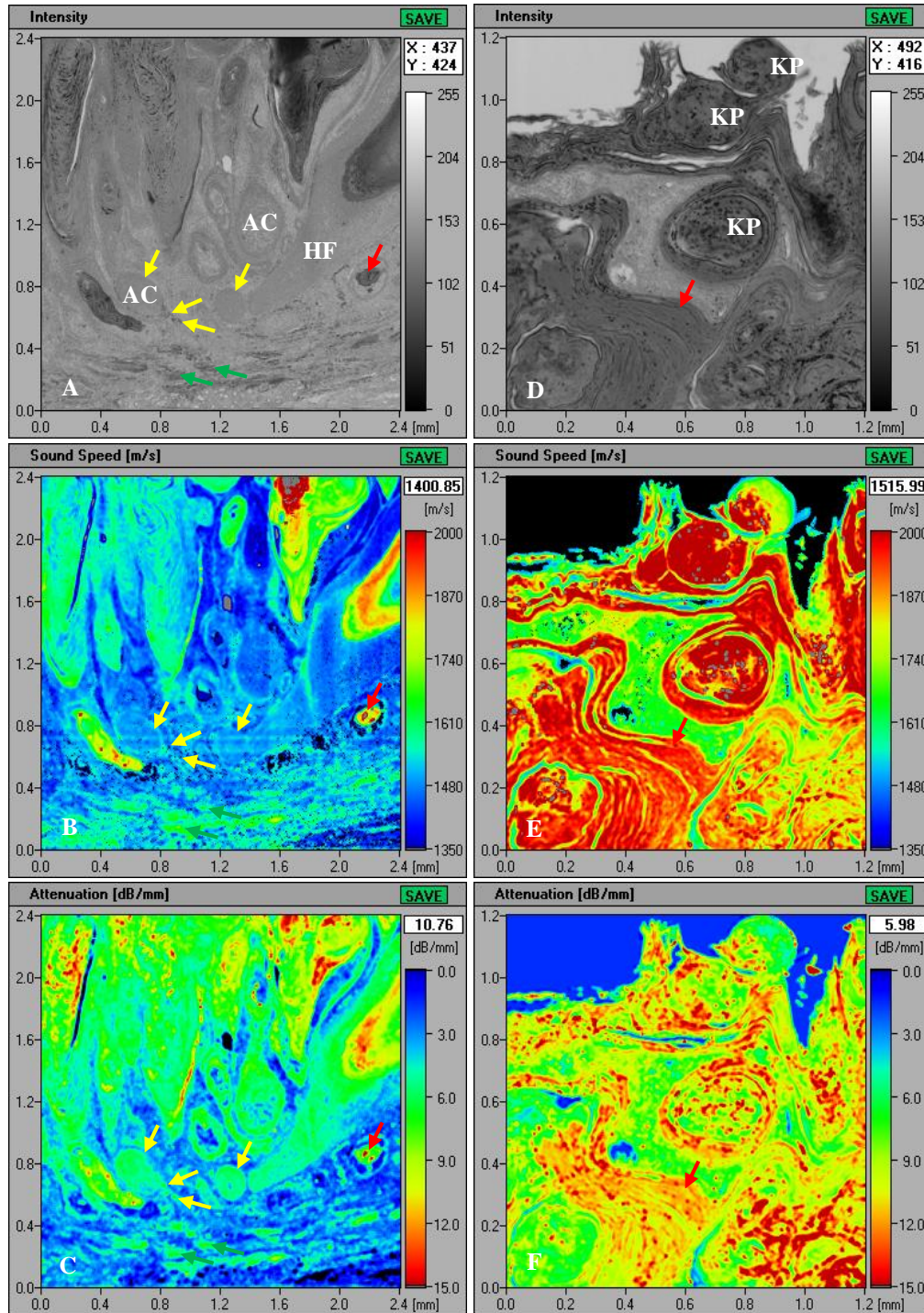
Figure 5.6: Acoustic images of the squamous cell carcinoma: the active carcinoma cells (left column) and the keratinized region (right column). Intensity (A, D), sound speed (B, E) and attenuation (C, F). *Yellow arrow: squamous cell carcinoma. Green arrow: desmoplastic stroma. Red arrow: keratin formation. KP: keratinous pearls.*

Figure 5.6 represents detailed images of the keratinized region (right column) and the active carcinoma cells (left column) along with the sound speed and attenuation distribution in those regions. The abnormal squamous cell specified by a yellow arrow are readily distinguished and have the speed of sound of 1470 ±40 m/s (B) and attenuation 7.1 ±1.8 dB/mm (C). The attenuation value (6.2 ±3.6 dB/mm) is similar to that measured by other researchers [85]. Also, we can differentiate the desmoplastic stroma (marked by green arrow) formed around the tumour with other different types of cells with their own characteristics properties. This dense fibrosis (thickening of connective tissues) appears long shaped and exhibits a notable high SOS (1650 ±30 m/s) and AOS (8.6 ±0.6 dB/mm).

Keratinous pearls (KP) on Figure 5.6 (D) are very well-defined structures showing sharp round border with layers and the keratin content inside. The speed of sound and attenuation values were remarkably higher to those in carcinoma cells. The measured values were 1990±60 m/s for SOS (E) and 13.7 ±1.0 dB/mm for AOS (F).

5.1.3 Basal Cell Carcinoma

Figure 5.7 shows a typical superficial basal cell carcinoma. The lesion area in this cancer type is often limited to the epidermis and the papillary layer and, therefore, all the primary skin structure is visible. Several nests of basaloid cells (BC) are located subepidermally with a clear connection with the basal layer of the epidermis (E). They are shown as dense well-delineated areas invaded partially into the papillary dermis (PD). On the acoustic image, the lesion appears as a dark round tumour cluster with low reflectivity. Also, some skin structures such as sebaceous gland is present in the image. When compared to the healthy epidermis (Figure 5.1), the epidermis in the BCC lesion demonstrates increased thickness. To that extent, the dermal papillae disappear.
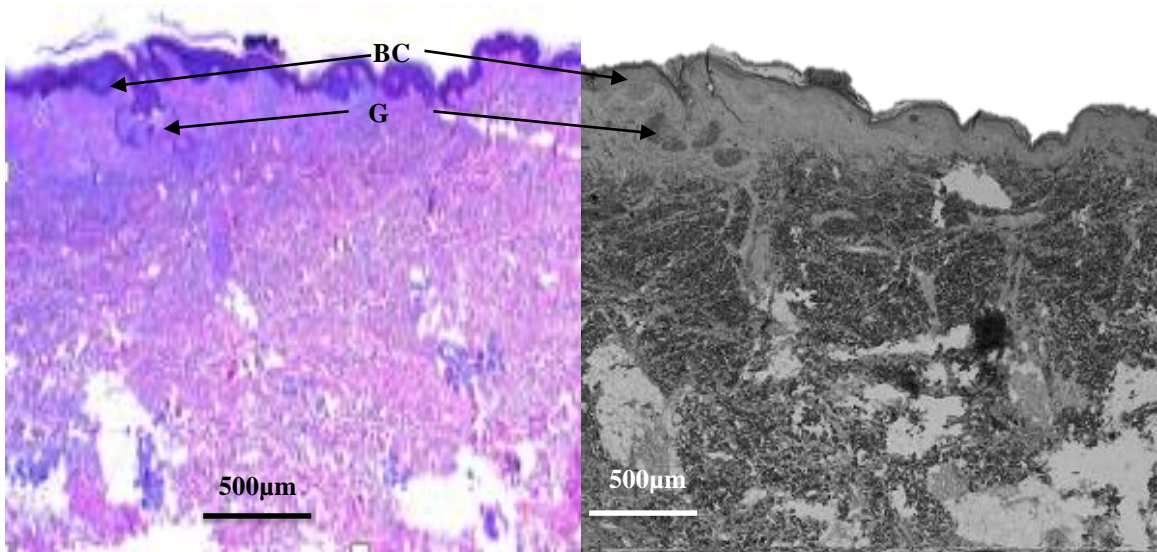
Figure 5.7: Basal cell carcinoma. H&E image (left) and the acoustic image of the same area (right). *BC: basaloid cell, G: sebaceous glands.*
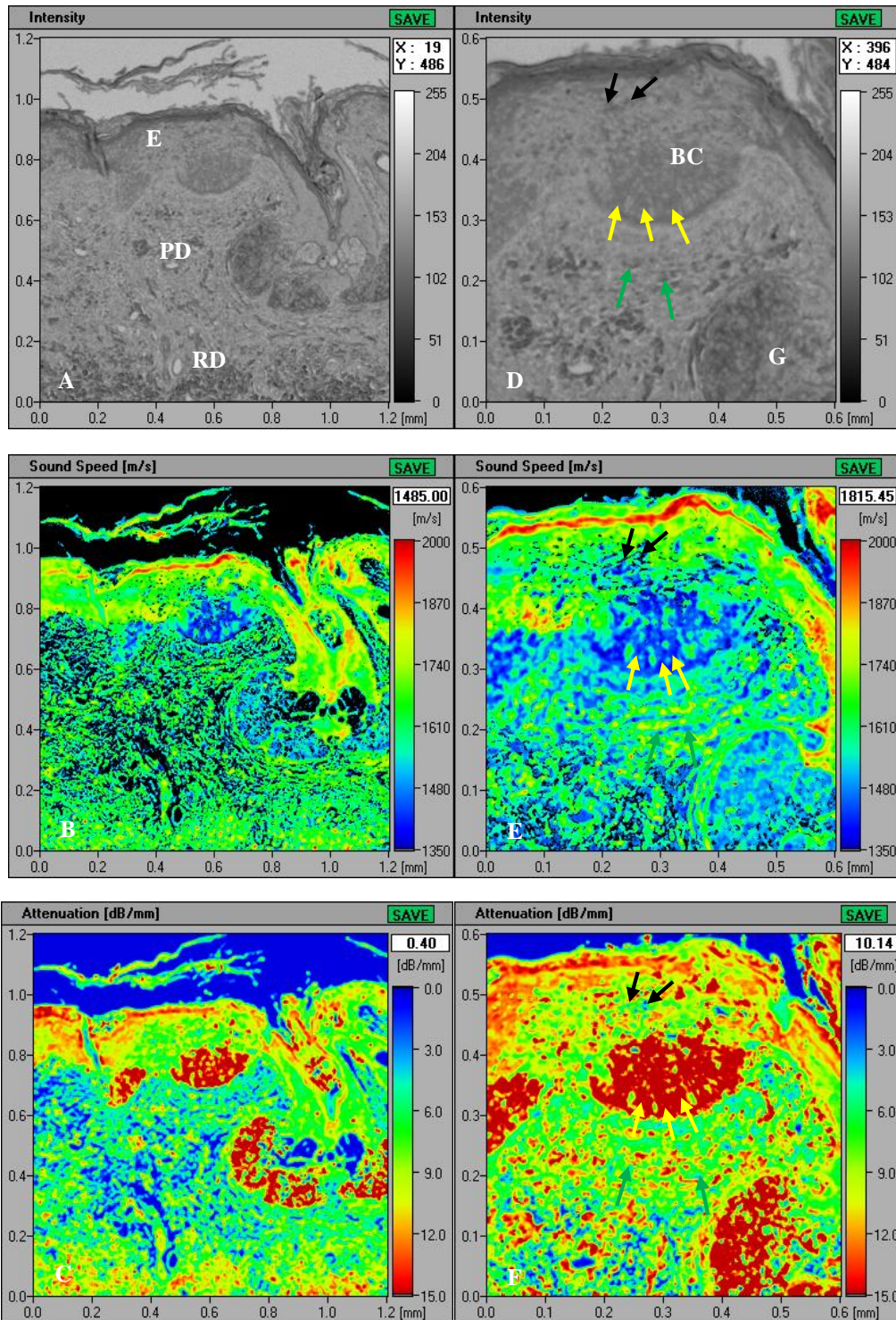
Figure 5.8: Acoustic images (A, D), sound speed (B, E) and attenuation (C, F) of basal cell carcinoma. *Yellow arrow: basal cell carcinoma. Black arrow: epidermal dysplasia. Green arrow: elastotic sun damaged collagen fibres. E: epidermis, PD: papillary dermis, RD: reticular dermis. BC: basaloid cell, G: sebaceous glands.*
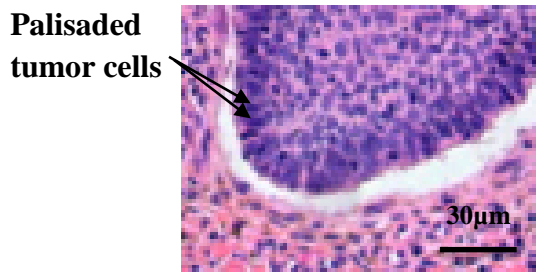
Figure 5.9: Palisading arrangement of cancer cells at the periphery of tumor.

Figure 5.8 (A) demonstrates the same area with higher magnification and ultrasonic properties mapping. The obtained acoustic images present more fine details that allow us to discriminate various type of cells. As we can see the tumour cells (shown by yellow arrows) are distributed in the palisaded pattern at the periphery of the neoplasm cluster, whereas the cells located in the middle of the lesion are irregularly disposed of as spindle-shaped. The presence of peripheral palisaded cells is a very characteristic feature of basal cell carcinoma (Figure 5.9) [114]. These cells display a remarkable decrease in the sound speed compared to the healthy tissue with an average value of 1430 ± 30 m/s and a significant increase in the attenuation with mean of 22.6 ± 1.6 dB/mm.

It is worth to note that the sebaceous gland looks very similar to the basaloid structure as round- shaped structure and demonstrates similar attenuation (24.4 ± 2.3 dB/mm) and slightly higher sound speed (1510 ± 30 m/s).

The basaloid cell is surrounded by elastotic (indicated by green arrow) occurred as a result of sun damage collagen fibres. These abnormal elastin shows a slightly high SOS (around 1500 ± 30 m/s) and extremely low AOS (around 5.9 ± 0.6 dB/mm) comparing to healthy collagen. (Figure 5.8- B, C). However, in the reticular dermis, no valuable change in the acoustic properties is been recorded that agrees with an early stage of carcinoma that has been used in this study.

The epidermal layer is dysplastic associated with chronic sun damage and premalignant change in the skin preceding the development of cancer. Epidermal dysplasia displays an increase in the attenuation parameter with an average value of 11.1 ±0.5 dB/mm and a decrease in the speed of sound with mean of 1660 ± 20 m/s compared to the healthy skin properties in Figure 5.8 (F) and (E) respectively.

5.1.4 Melanoma

Figure 5.10 illustrates the typical case of nodular malignant melanoma (Clark's level V). The vertical growth pattern demonstrates the invasion of the tumour inside the dermis to the last layer of the skin (subcutaneous tissue) with the destruction of the epidermal-dermal junction as can be seen in both acoustic and optical images. Hence, we are unable to competently define the epidermal and dermal layers as two separate regions. As well as, we can appoint the irregularity of the outer border of the lesion on the acoustic image that is in good concordance with H&E, and that indicated the invasiveness of melanoma.
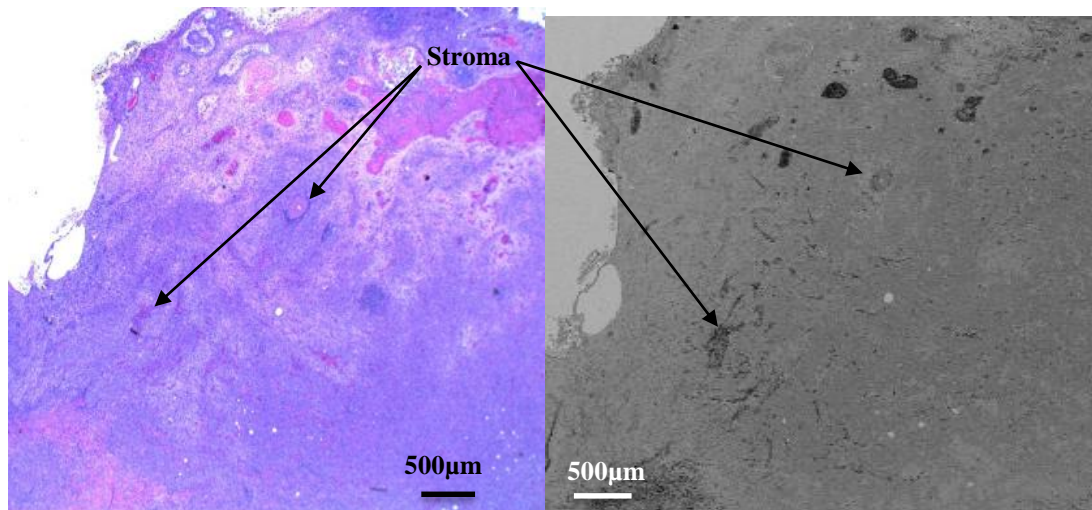
Figure 5.10: Comparison of acoustic image of malignant melanoma (right) with its corresponding H&E image (left).

Connective tissue and blood vessels (stroma) appear all over the centre representing the structure of the supportive tissue for the tumour. They are shown as pink-stained features on the left side of Figure 5.9 and as dark gray on the acoustic image. Also, the dermal component of the invasive melanoma offers plentiful of single atypical melanocytes and is entirely free keratin features that occurred in SCC.
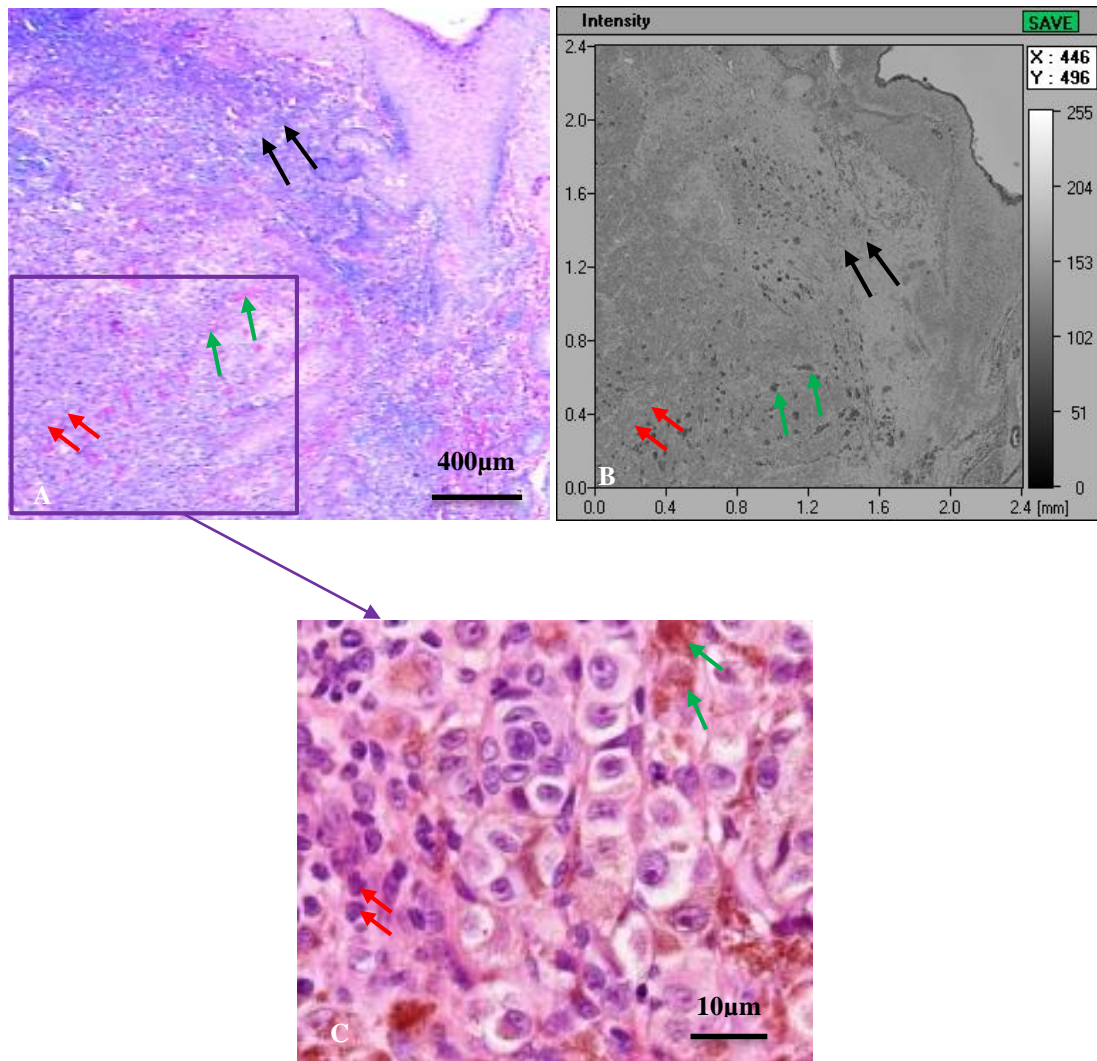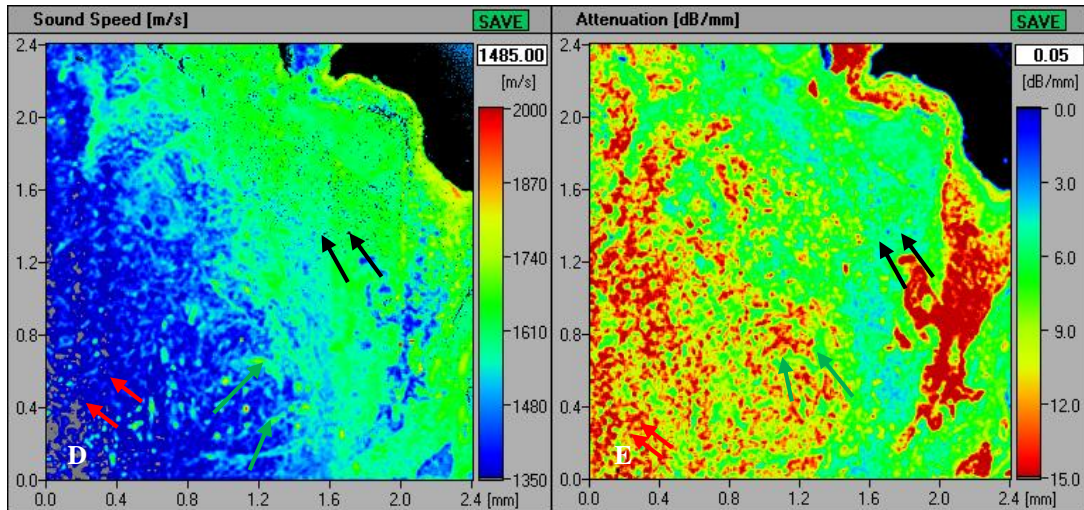
Figure 5.11: High-resolution acoustic image (B) of nodular malignant melanoma with sound speed (D) and attenuation (E) distribution. The image (A) represents the corresponding optical and its higher magnified image (C). *Red arrow: tumour cells. Black arrow: follicular squamous cells. Green arrow: stroma.*

Figure 5.11 shows details of the melanoma lesion with a higher resolution allowing distinguish individual cells. Melanoma cells in the centre of the lesion shown by red arrow demonstrate the remarkable low speed of sound and noticeable high attenuation (D-E). The averaged values are 1340 ± 70 m/s for sound speed and 22.0 ± 1.7 dB/mm for attenuation. In the optical image (A-C), melanoma cells appear as small violet stained cells while in the acoustic image (B) as light gray coloured features. The tumour cells are surrounded by loose stroma, indicated by the green arrow, with distinct acoustic properties: speed of sound (1640 ± 30 m/s) and attenuation (7.5 ± 0.7dB/mm). Another type of cells, follicular squamous cells are differentiated from melanoma cells and connective tissue by their acoustic properties (SOS and AOS) on the colour coded images as they look similar in the grayscale intensity image (B). The follicular squamous cells appear as dark blue dots in velocity image (D) with low attenuation (light blue colour) in (E).

5.1.5 Discussion of Sound Speed and Attenuation Data

High- resolution acoustic microscopy allows visualizing all fine skin features without the need to stain the tissue as the image contrast mechanism is based on the variations of the visco-elastic properties of the skin elements. The acoustic images show good concordance with the traditional H&E stained optical images that are the gold standard in today's histopathology. Besides imaging, the acoustic microscopy offers the possibility to quantify the skin characteristics and map them by measuring the properties of the individual cell. Table 5.2 represents the averaged values of the acoustic properties of the healthy skin structures and skin cancer lesions.

Table 5.2: Acoustic properties of healthy skin structures and skin cancers.

Skin Feature	Sound Speed (m/s)	Attenuation (dB/mm)
Healthy Skin		
Epidermis	1720 ± 30 m/s	9.1 ± 0.7 dB/mm
Papillary Dermis	1650 ± 30 m/s	10.0 ± 0.8 dB/mm
Reticular Dermis	1790 ± 50 m/s	11.7 ± 1.0 dB/mm
Squamous Cell Carcinoma		
Keratinous Pearls	2120 ± 70 m/s	13.7 ± 0.7 dB/mm
Tumor Squamous Cells	1470 ± 40 m/s	7.1 ± 1.8 dB/mm
Desmoplastic Stroma	1650 ± 30 m/s	8.7 ± 0.5 dB/mm
Basal Cell Carcinoma		
Basaloid Cells (Tumor Cells)	1420 ± 40 m/s	22.4 ± 1.3 dB/mm
Epidermal Dysplasia	1660 ± 20 m/s	12.0 ± 0.5 dB/mm
Elastotic Stroma	1510 ± 30 m/s	5.8 ± 0.6 dB/mm
Sebaceous Glands	1520 ± 30 m/s	24.8 ± 2.0 dB/mm
Melanoma		
Melanoma cells	1360 ± 50 m/s	20.7 ± 1.4 dB/mm
Stroma	1620 ± 30 m/s	8.7 ± 0.9 dB/mm
Follicular Squamous Cells	1560 ± 20 m/s	4.3 ± 0.6 dB/mm
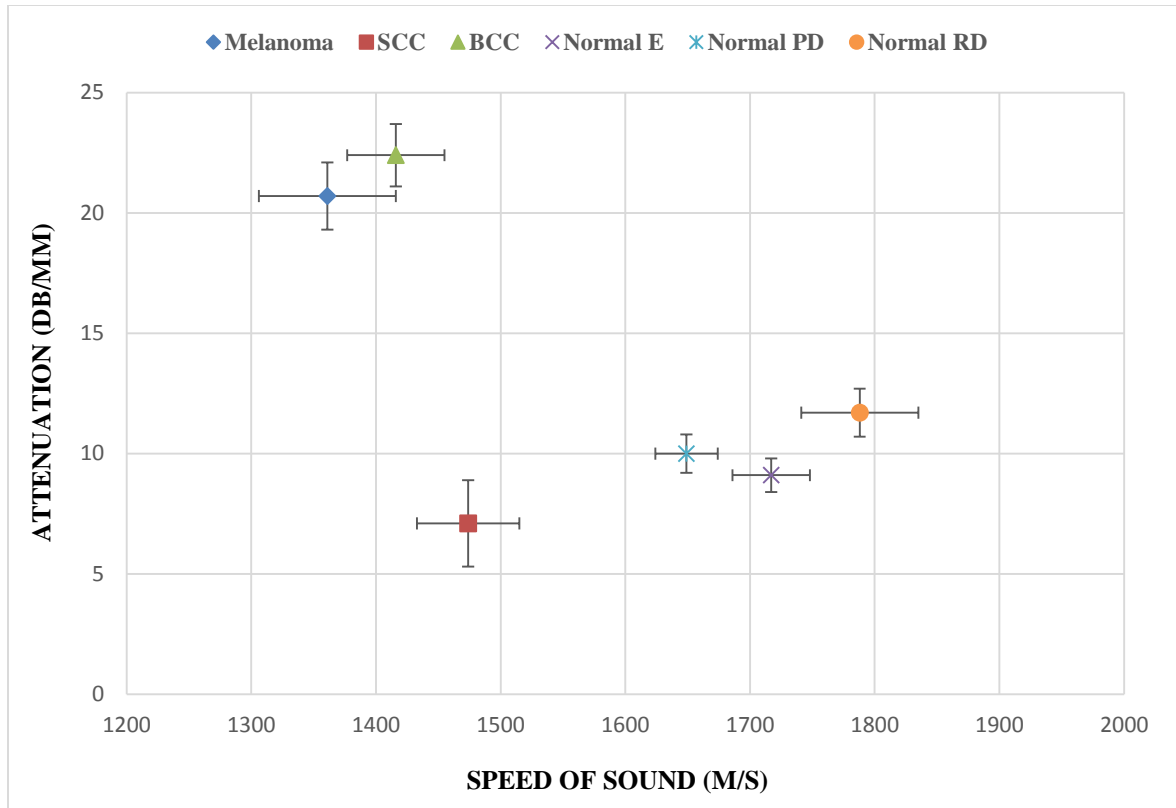
Figure 5.12: The plot representing ultrasonic properties of the healthy and skin cancer structures. *SCC: squamous cell carcinoma, BCC: basal cell carcinoma, Normal E, PD, RD: normal epidermis, papillary dermis, reticular dermis respectively.*

Figure 5.12 shows the distribution of the ultrasonic properties of melanoma and non-melanoma skin cancer (SCC, BCC) cells compared to healthy skin properties. There is a significant difference in speed of sound (SOS) and attenuation of sound (AOS) among tumour cell types and normal tissues. These measurements show that SOS in normal skin ranges from1600 m/s to 1850 m/s, and in the skin, cancer lesions vary from 1300 m/s to 1520 m/s depending on the cancer type. Melanoma cells demonstrate the lowest sound speed values (1360 ± 50 m/s). This difference between the sound speed of normal and pathological skin is in line with previous publications showing by atomic force microscopy (AFM) that cancer cells appear softer than normal cells [115]–[118]. It is known that the sound speed is higher in cells than in isolated nuclei. However, the cancer cells typically

have enlarged nuclei; often they take all cell space. Thus, the observed lower sound speed in cancer cells can be explained by increased nuclei size [119].

It is important to note cancer cells biomechanics is not understood fully yet. Most cancer lesions are more rigid than surrounding tissue [44], [120]–[123]. It was shown that cancer cells exhibit a high speed of sound in cell cluster compared to the single cell [85]. However, the individual cancer cells are found to be much softer than the healthy cells [85], [115]–[118].

This paradox can be explained by an increase in developing of stroma structures such as blood vessels and collagen content during cancer progression [121]. Also, there is a considerable increase in cancer cell heterogeneity at the late tumour stages [118]. Weder et al. [121] demonstrated that melanoma cells progression is associated with a decrease in stiffness, while further advancement to metastatic melanoma is accompanied by an increase in the cells stiffness. Thus, the overall increase of stiffness in cancer lesions occur due to the increased plasticity of the cancer cells and developed supportive stroma structures that surrounds the lesion.

On the other side, both melanoma and BCC show high sound attenuation about 20.7 ±1.4 dB/mm and 22.4 ±1.3 dB/mm respectively, compared to healthy tissue. These values are in correlation with other results obtained by tone-burst scanning acoustic microscopy [88] and quantitative ultrasound [7] technique.

Among studied skin cancers, each type has its own combination of the ultrasonic properties. The high-resolution acoustic imaging enforced with quantitative tissue analysis

can equip the pathologist with additional information assisting him to lean to specific diagnosis in doubtful cases.

This significant difference in both sound speed and attenuation in healthy skin and cancer lesion can be used as a basis for discriminating between the healthy tissue and the cancer lesion to validate the margin status during surgery to ensure all cancerous tissue has been removed.

Although this study shows a strong correlation between acoustic microscopy imaging and optical histopathology results, the research was limited by the number of samples provided and the availability of various pathological cases. Therefore, the usefulness of acoustic properties to distinguish between different types of skin cancer should be further evaluated.

5.2 Evaluation of the Acoustic Impedance of Human Skin

5.2.1 Estimating AI of Skin from Experimental SOS Values

The obtained values of the sound speed in skin Table 5.2 were used to estimate the acoustic impedance of skin layers. However, the speed of sound of melanoma cells was not counted for acoustic impedance estimation of melanoma as at lower frequency (50 MHz) individual cells cannot be resolved. The measured sound speed for melanoma tumor region is about 1530 ± 50 m/s. The acoustic impedance is the product of sound speed and density. The density for both healthy skin and melanoma lesion was also been measured based on the Archimedean principle using Sartorius balance and a density determination kit. This density is similar to the literature measured value [124]. Assuming that the density of all layers is constant the characteristic acoustic impedance can be estimated (Table 5.3).

Table 5.3: Acoustic impedance estimation for healthy skin and melanoma skin cancer.

Acoustic Properties	Epidermis	Papillary Dermis	Reticular Dermis	Melanoma
Measured Average Sound Speed (m/s)	1720 ± 30	1650 ± 30	1790 ± 50	1530 ± 50
Density (g/cm^3)	1.09	1.09	1.09	1.09
Estimated Characteristic Acoustic Impedance (MPa.s/m^3)	1.87 ± 0.03	1.80 ± 0.03	1.95 ± 0.05	1.67 ± 0.03

5.2.2 Acoustic Impedance Measurements on Thickly Sliced Skin

The recently proposed method of acoustic microscopy [88] that measures the acoustic impedance of the tissue has been used to investigate properties of thickly cut skin tissues.Figure 5.13 below shows on the left the acoustic intensity image of the cross-section of thickly sliced (0.5 mm) healthy with 50 MHz transducer. We can point the existence of the hair shafts at the skin surface. Also, we can define the sebaceous glands that are shown as features with increased brightness. Small bright dots seen through the image correspond to the small air bubbles trapped due to the low compatibility of the tissue with the PS substrate and poor wetting of the PS substrate. The distribution of the characteristic acoustic impedance in healthy skin is represented on the Figure 5.13, right. The values of the characteristic acoustic impedance vary from 1.5 to 2 MN.s/m^3.
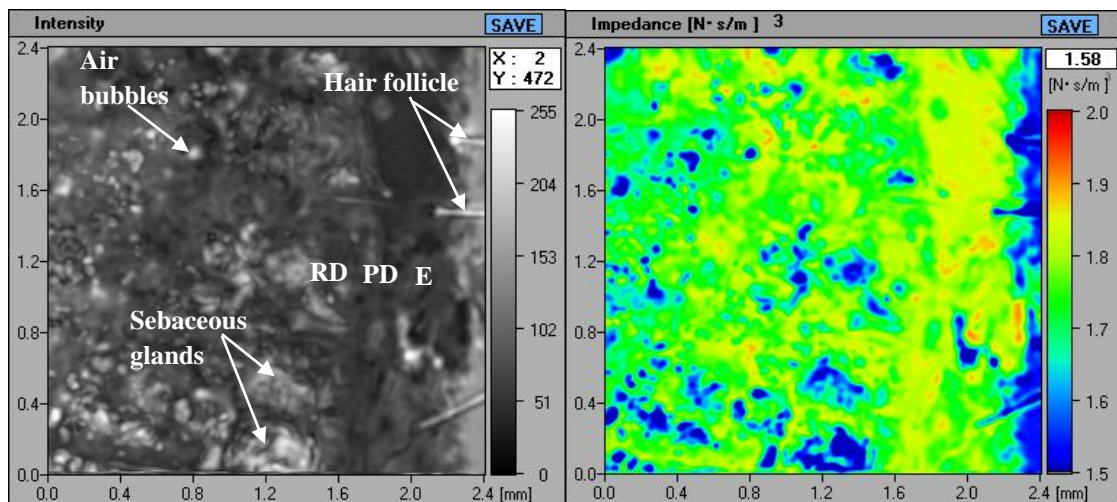
Figure 5.13: Intensity image (left) and the acoustic impedance distribution (right) of healthy skin made with PS substrate.

The measurement of the values of acoustic impedance (AI) for each layer was done by choosing a ROI and calculate the mean of 20 pixels in there with the standard deviation. The ROI was chosen away from the area that contains PBS (referred to blue colour with

Z_{PBS}=1.54 MN.s/m^3) and air bubbles acoustic impedance values to minimize the error. All measured values are represented as the mean ± SD in Table 5.4 below.

Table 5.4: The acoustic impedance of healthy skin measured with the untreated PS.

Skin Layers	Averaged Characteristic AI (MN.s/m^3)
Epidermis	1.82 ±0.03
Papillary Dermis	1.77 ±0.03
Reticular Dermis	1.81 ± 0.02
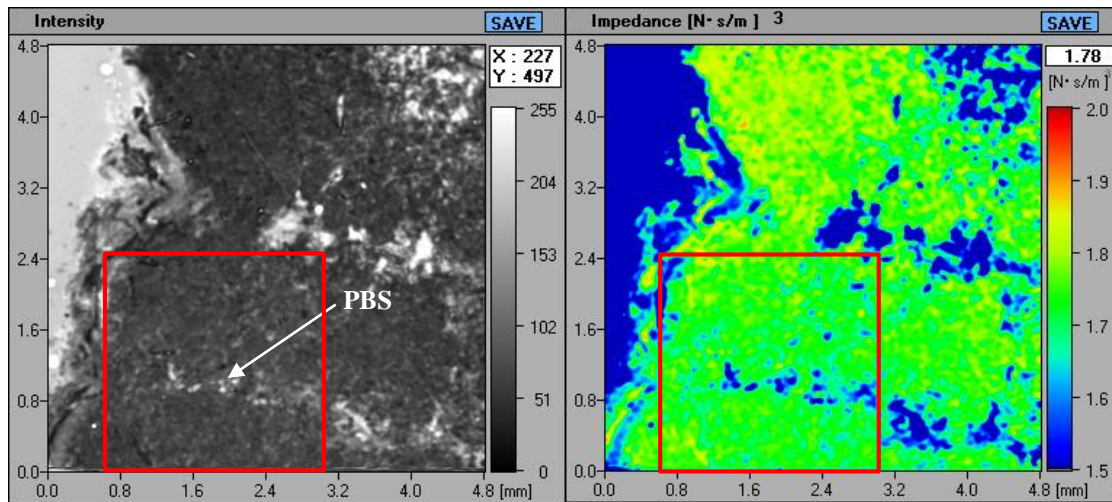
Figure 5.14: Acoustic image (left) and the acoustic impedance distribution (right) of melanoma lesion. The red box with a field of view 2.4×2.4 mm^2 marks the melanoma tumour region where the measurement is acquired.

Figure 5.14 shows on the left the intensity image of the skin with melanoma lesion. We marked the loss of fine textures comparing to the healthy thickly skin. These features relate to the characteristic of thick melanoma that has been demonstrated before using burst-mode of SAM where abnormal tissue has less surface roughness than the normal tissue [88]. Although acoustic impedance mode shows some features in the skin, it offers much lower

resolution compared to the sound speed mode that permits the cellular imaging of the skin with 320 MHz transducer. Therefore, it is impossible to recognize melanoma cells on the images obtained with 50 MHz transducer.

The distribution of the acoustic impedance in the melanoma lesion marked by a red square is shown in Figure 5.14, right. The average characteristic acoustic impedance is 1.69 ± 0.03 MN.s/m^3. Thus, the acoustic impedance is lower in melanoma than in the healthy skin.

5.2.3 Surface Treatment of Polystyrene Substrate

The acoustic impedance measurement require the close contact of the tissue with the plastic substrate to achieve the good quality images and precise measurements. The polystyrene has low surface energy that prevents wetting the plastic surface with PBS [107], [125] . Plasma discharges in oxygen are often used to increase the surface energy, they are known to produce new oxygen-containing chemical functions at the surface and to increase the wettability [126]. To improve wettability of the PS and to increase the contact with the specimen, the surface of the PS substrate was treated beforehand by a plasma surface treatment.
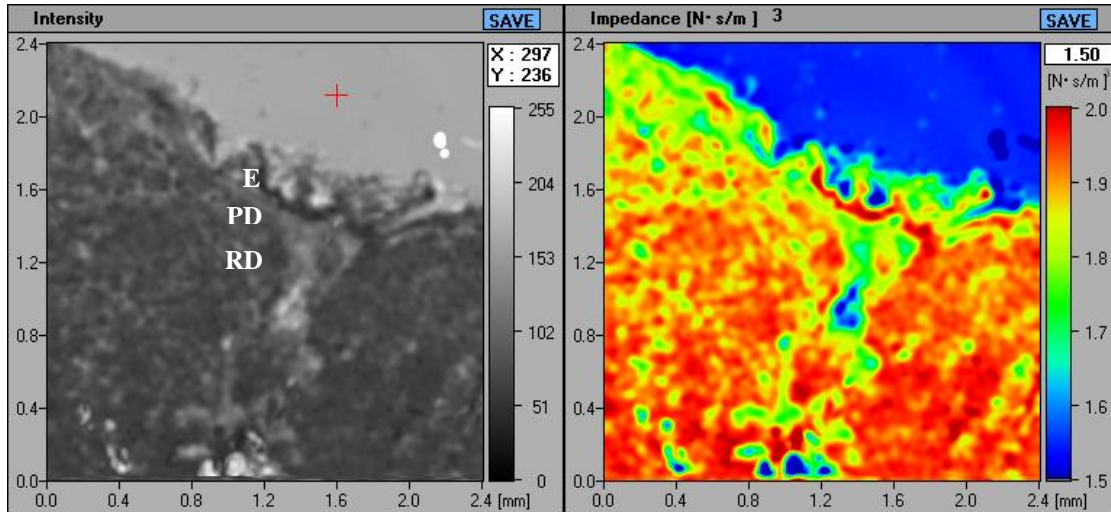
Figure 5.15: Intensity image (left) and the acoustic impedance distribution (right) of healthy skin made with plasma treated PS substrate.

Figure 5.15 shows a C-scan image of the cross-section of the healthy skin tissue (left) and its corresponding distribution of the acoustic impedance (right). These images were obtained with the plasma-treated PS substrate to improve the wetting of the increase wettability of the polystyrene surface. The scanning was performed directly after the treatment. As we can see, the acoustic image shows better contact between the sample and the substrate, less trapped air bubbles and PBS are visible at the image.

Measured values of acoustic impedance for each layer are represented in Table 5.5 below as the mean ± SD. It is important to note that acoustic impedance measured with the treated substrate shows higher acoustic impedance for all three skin layers comparing to the measurements made with the untreated polystyrene values.

Table 5.5: The acoustic impedance of healthy skin measured with the plasma treated PS.

Skin Layers	Averaged Characteristic AI (MN.s/m^3)
Epidermis	1.85 ±0.03
Papillary Dermis	1.80 ±0.05
Reticular Dermis	1.93 ±0.02

5.2.4 Acoustic Impedance Data Analysis and Discussion

Figure 5.16 shows the quantitative assessment of acoustic impedance for all layers in the healthy skin and for melanoma lesion. The acoustic impedance of melanoma lesion is statistically different from the acoustic impedance of healthy skin ($p<0.05$). The tumour region is marked with a significant decrease in acoustic impedance (1.69 ±0.03 MN.s/m^3). Other researchers also demonstrate that acoustic impedance of cancer cells is much lower than normal cells using acoustic impedance imaging method [83]. This approach indicates that the acoustic impedance measurement could be used to distinguish between healthy and cancerous regions in excised skin tissue. It is shown that the nucleus has lower acoustic impedance than the surrounding cytoskeleton in the cytoplasm [87]. Thus, cancer cells may have less cytoskeleton (actin filaments and microtubules) and exhibit low stiffness than healthy cells. It is still unclear the cause of the decreased stiffness (and, correspondingly, sound speed and acoustic impedance) in melanoma lesion.
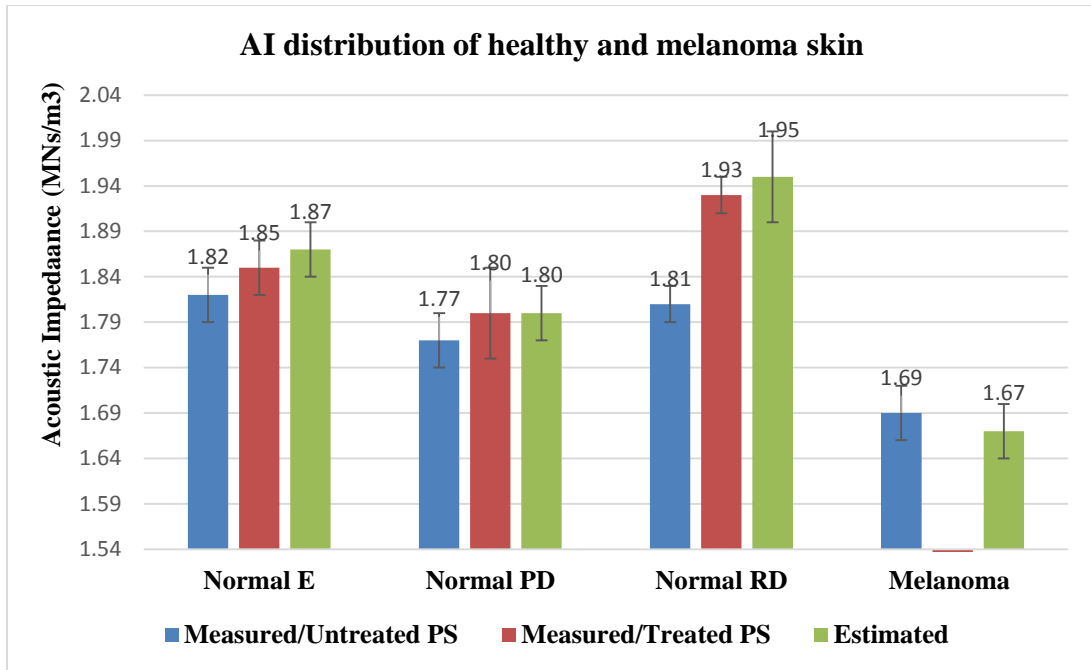
Figure 5.16: Measured and estimated acoustic impedance of the healthy and melanoma skin. *E: epidermis, PD: papillary dermis, RD: reticular dermis, PS: polystyrene.*

The estimated data for the acoustic impedance are slightly higher than measured. This may arise from the error of measurements as well as from the measured density value. Nevertheless, melanoma shows significantly lower stiffness in both sound speed and acoustic attenuation measurements comparing to healthy skin.

The obtained data will be useful for modelling the acoustic distribution in the skin tissue for a new theoretical model (B to Z analysis) in order to make the ultrasonic method practically useful in disease diagnosis [127].

Figure 5.16 also shows the difference in acoustic impedance of the skin acquired untreated and plasma treated polystyrene plastic substrate. Treating the PS surface leads to the increase in AI. We assume that this happens due to the fact that the contact between the tissue and the substrate improves to ensure the accuracy of measurement for acoustic impedance. The most statistically significant difference in the AI values is observed for the

reticular dermis (p<0.05). This surface treatment technique has been used by other researchers for resolution improvement of cerebellum tissue imaging [84], [107], [125]. The challenge is that the hydrophilic property of PS is time sensitive and lasts about one hour after treatment. Thus, the observation should be completed directly after the substrate treatment.

Skin elastic characteristics are different for each layer, and therefore, we can expect the acoustic impedance values will vary for each skin layer; what is proved in this study as shown in Figure 5.16. The measured acoustic impedance values were compared with the estimated ones that were calculated using the measured sound speed and measured skin density value. As shown, the estimated values for the AI agrees better with values obtained after plasma treatment.

CHAPTER 6

CONCLUSIONS AND RECOMMENDATIONS

Diagnostic ultrasound is widely used in today's medicine. However, it has limited application to diagnose specific skin pathologies namely skin cancer. Easy access to the skin to biopsy and excision made skin underexplored using ultrasonic diagnostic imaging. Ultrasonic and atomic force microscopy show that skin cancer cells have lower stiffness compared to healthy cells. The speed of sound and acoustic impedance measured by the acoustic microscopy are the indirect measurements of the elastic modulus.

Scanning acoustic microscopy provides the following benefits over light microscopy: (1) acoustic image reflects the tissue elasticity, (2) acoustic imaging does not need any special tissue preparation or staining.

This study aim to investigate whether the high-resolution acoustic microscopy has the potential for identifying and quantitatively classifying skin cancers. The motivation for this work came from the biomedical industry that needs useful non-invasive method for detection melanoma to reduce misdiagnosis rate and lower mortality from cutaneous melanoma.

Basal cell carcinoma, squamous cell carcinoma and malignant melanoma were investigated using acoustic microscopy method at 320 MHz and 50 MHz frequency. It was demonstrated that acoustic images show good correlation with H&E stained optical images of the subsequent histological slides. The ultrasonic image reveals the overall skin architecture and all fine details of the skin structure including individual cells.

The algorithm for quantitative evaluation of the human tissue was adapted for the measurements of properties of individual cell. Using advanced frequency domain of signal analysis, it is possible to calculate the speed of sound and attenuation in the tissue and map the distribution of these parameters. The speed of sound in tissues and cells correlate with tissue elasticity indicating their biomechanical properties. The elasticity varies according to the tissue type and its composition as well as collagen or elastic fibres, ground substances, and the cytoskeleton contributes to this elasticity.

Acoustic properties of the epidermis and dermis in healthy skin were measured as well as the acoustic properties of the skin cancer neoplasms. It was shown that cells of all three types of skin cancer have the sound speed significantly lower compared to the healthy skin cells. The melanoma cells have the lowest values of sound speed, 1360 ± 50 m/s while basal cell carcinoma and squamous cell carcinoma have 1420 ± 40 m/s and 1470 ± 40 m/s correspondingly. The sound speed in the healthy skin was found to be 1720 ± 30 m/s for epidermis, 1650 ± 30 m/s for papillary dermis, and 1790 ± 50 m/s for reticular dermis.

The measured attenuation in melanoma and BCC lesions were found to be significantly higher than in healthy skin, 20-23 dB/mm compared to 9-11.7 dB/mm, correspondingly. The squamous cell carcinoma shows attenuation similar to that in healthy skin cells. This significant difference in the acoustic properties of normal and melanoma cells allows distinguishing between the healthy area and the lesion. These findings may work as the basis for the new ultrasonic method to assist the surgeon in verifying if all cancer lesion has been removed.

The estimation of the acoustic impedance based on the measured sound speed in thin histological slides correlate well with the measured values of the acoustic impedance performed on the thick samples of the skin. Treatment of the surface of the polystyrene substrate to increase surface energy and improve the contact between the substrate and the sample lead to significant increase in acoustic impedance values due to improved contact and eliminating the PBS buffer layer between the skin sample and the plastic. Values of the AI measured with the treated polystyrene have a better match with the estimated values. To our knowledge, based on an extensive literature review, no study has been found regarding acoustic impedance analysis for cutaneous carcinomas.

This study was not designed to assess the clinical utility of SAM in routine dermopathology practice. However, future studies with more significant number of subjects may offer the potential to substantially impact clinical practice if the results of this study are reproducible.

Future work should also include the comparison of melanoma properties with the properties of normal or abnormal nevus as distinguishing between the melanoic, and benign nevi is a challenging task for a dermatologist that require a lot of training and experience. Applying the method non-invasively by evaluating patients' skin nevi is another step toward the developing the non-invasive method for fast melanoma detection.

BIBLIOGRAPHY

[1]   R. R. Wickett and M. O. Visscher, "Structure and function of the epidermal barrier," *Am. J. Infect. Control*, vol. 34, no. 10 SUPPL., pp. 98–110, 2006.

[2]   K. Korotkov and R. Garcia, "Computerized analysis of pigmented skin lesions: A review," *Artif. Intell. Med.*, vol. 56, no. 2, pp. 69–90, 2012.

[3]   Z. Apalla, D. Nashan, R. B. Weller, and X. Castellsague, "Skin Cancer: Epidemiology, Disease Burden, Pathophysiology, Diagnosis, and Therapeutic Approaches," *Dermatol. Ther. (Heidelb).*, vol. 7, pp. 5–19, 2017.

[4]   G. Paolino, M. Donati, D. Didona, S. Mercuri, and C. Cantisani, "Histology of Non-Melanoma Skin Cancers: An Update," *Biomedicines*, vol. 5, no. 4, p. 71, 2017.

[5]   J. J. Bonerandi *et al.*, "Guidelines for the diagnosis and treatment of cutaneous squamous cell carcinoma and precursor lesions," *J. Eur. Acad. Dermatology Venereol.*, vol. 25, no. SUPPL. 5, pp. 1–51, 2011.

[6]   K. Andrėkutė, G. Linkevičiūtė, R. Raišutis, S. Valiukevičienė, and J. Makštienė, "Automatic Differential Diagnosis of Melanocytic Skin Tumors Using Ultrasound Data," *Ultrasound Med. Biol.*, vol. 42, no. 12, pp. 2834–2843, 2016.

[7]   H. Piotrzkowska-Wroblewska, J. Litniewski, E. Szymanska, and A. Nowicki, "Quantitative sonography of basal cell carcinoma," *Ultrasound Med. Biol.*, vol. 41, no. 3, pp. 748–759, 2015.

[8]   L. I. Petrella, H. de Azevedo Valle, P. R. Issa, C. J. Martins, J. C. Machado, and W. C. A. Pereira, "Statistical Analysis of High Frequency Ultrasonic Backscattered

Signals from Basal Cell Carcinomas," *Ultrasound Med. Biol.*, vol. 38, no. 10, pp. 1811–1819, 2012.

[9] L. I. Petrella, H. A. Valle, P. R. Issa, C. J. Martins, W. C. A. Pereira, and J. C. Machado, "Study of cutaneous cell carcinomas ex vivo using ultrasound biomicroscopic images," *Ski. Res. Technol.*, vol. 16, no. 4, pp. 422–427, 2010.

[10] K.-B. Tan *et al.*, "Simulators of Squamous Cell Carcinoma of the Skin: Diagnostic Challenges on Small Biopsies and Clinicopathological Correlation," *J. Skin Cancer*, vol. 2013, no. Mcc, pp. 1–10, 2013.

[11] A. Stratigos *et al.*, "Diagnosis and treatment of invasive squamous cell carcinoma of the skin: European consensus-based interdisciplinary guideline," *Eur. J. Cancer*, vol. 51, no. 14, pp. 1989–2007, 2015.

[12] P. S. Karia, J. Han, and C. D. Schmults, "Cutaneous squamous cell carcinoma: Estimated incidence of disease, nodal metastasis, and deaths from disease in the United States, 2012," *J. Am. Acad. Dermatol.*, vol. 68, no. 6, pp. 957–966, 2013.

[13] M. Rastgoo, R. Garcia, O. Morel, and F. Marzani, "Automatic differentiation of melanoma from dysplastic nevi," *Comput. Med. Imaging Graph.*, vol. 43, pp. 44–52, 2015.

[14] X. Wortsman, "Sonography of the Primary Cutaneous Melanoma: A Review," *Radiol. Res. Pract.*, vol. 2012, pp. 1–6, 2012.

[15] B. Bandarchi, C. A. Jabbari, A. Vedadi, and R. Navab, "Molecular biology of normal melanocytes and melanoma cells," *J. Clin. Pathol.*, vol. 66, no. 8, pp. 644–

648, 2013.

[16]   N. Razazzadeh and M. Khalili, "Classification of the Pigmented Skin lesions in Dermoscopic Images by Shape Features Extraction," *Ijmec*, vol. 5(15), no. 15, pp. 2151–2156, 2015.

[17]   M. Balu *et al.*, "Distinguishing between benign and malignant melanocytic nevi by in vivo multiphoton microscopy," *Nat. Rev. Cancer*, vol. 13, no. 2, pp. 83–96, 2013.

[18]   L. Machet *et al.*, "Preoperative Measurement of Thickness of Cutaneous Melanoma Using High-Resolution 20 MHz Ultrasound Imaging: A Monocenter Prospective Study and Systematic Review of the Literature," *Ultrasound Med. Biol.*, vol. 35, no. 9, pp. 1411–1420, 2009.

[19]   E. M. Finley, "The principles of mohs micrographic surgery for cutaneous neoplasia.," *Ochsner J.*, vol. 5, no. 2, pp. 22–33, 2003.

[20]   M. MOGENSEN and G. B. E. JEMEC, "Diagnosis of Nonmelanoma Skin Cancer/Keratinocyte Carcinoma: A Review of Diagnostic Accuracy of Nonmelanoma Skin Cancer Diagnostic Tests and Technologies," *Dermatologic Surg.*, vol. 33, no. 10, pp. 1158–1174, 2007.

[21]   A. Casari, J. Chester, and G. Pellacani, "Actinic Keratosis and Non-Invasive Diagnostic Techniques: An Update," *Biomedicines*, vol. 6, no. 1, p. 8, 2018.

[22]   R. B. Oliveira, M. E. Filho, Z. Ma, J. P. Papa, A. S. Pereira, and J. M. R. S. Tavares, "Computational methods for the image segmentation of pigmented skin lesions: A review," *Comput. Methods Programs Biomed.*, vol. 131, pp. 127–141, 2016.

[23] C. Fink and H. A. Haenssle, "Non-invasive tools for the diagnosis of cutaneous melanoma," *Ski. Res. Technol.*, vol. 23, no. 261, pp. 261–271, 2017.

[24] M. Ahmed Sheha, M. S. Mabrouk, and A. Sharawy, "Pigmented Skin Lesion Diagnosis by Automated Imaging System," *J. Bioeng. Biomed. Sci.*, vol. 6, no. 1, pp. 1–8, 2015.

[25] N. Eisemann *et al.*, "Non-melanoma skin cancer incidence and impact of skin cancer screening on incidence," *J. Invest. Dermatol.*, vol. 134, no. 1, pp. 43–50, 2014.

[26] E. D. O. Barcaui, J. Piñeiro-maceira, and C. B. Barcaui, "High - frequency ultrasound (22MHz) in the evaluation of malignant cutaneous neoplasms," vol. 6, no. 2, pp. 105–110, 2014.

[27] V. Kučinskiene, D. Samuleniene, A. Gineikiene, R. Raišutis, R. Kažys, and S. Valiukevičiene, "Preoperative assessment of skin tumor thickness and structure using 14-MHz ultrasound," *Med.*, vol. 50, no. 3, pp. 150–155, 2014.

[28] K. Andrekute, S. Valiukeviciene, R. Raisutis, G. Linkeviciute, J. Makstiene, and R. Kliunkiene, "Automated estimation of melanocytic skin tumor thickness by ultrasonic radiofrequency data," *J. Ultrasound Med.*, vol. 35, no. 5, pp. 857–865, 2016.

[29] D. Jasaitiene, S. Valiukeviciene, G. Linkeviciute, R. Raisutis, E. Jasiuniene, and R. Kazys, "Principles of high-frequency ultrasonography for investigation of skin pathology," *J. Eur. Acad. Dermatology Venereol.*, vol. 25, no. 4, pp. 375–382, 2011.

[30] I. F. Canedo, M. De Troya Martín, R. Fúnez Liébana, F. R. Ruiz, G. Blanco Eguren,

and N. Blázquez Sánchez, "Preoperative 15-MHz Ultrasound Assessment of Tumor Thickness in Malignant Melanoma," *Actas Dermosifiliogr*, vol. 104, no. 3, pp. 227–231, 2013.

[31]   T. Hinz *et al.*, "Preoperative characterization of basal cell carcinoma comparing tumour thickness measurement by optical coherence tomography, 20-MHz ultrasound and histopathology," *Acta Derm. Venereol.*, vol. 92, no. 2, pp. 132–137, 2012.

[32]   T. Gambichler *et al.*, "Preoperative ultrasonic assessment of thin melanocytic skin lesions using a 100-MHz ultrasound transducer: A comparative study," *Dermatologic Surg.*, vol. 33, no. 7, pp. 818–824, 2007.

[33]   M. Vogt, J. Opretzka, C. Perrey, and H. Ermert, "Ultrasonic microscanning," *Proc. Inst. Mech. Eng. Part H J. Eng. Med.*, vol. 224, no. 2, pp. 225–240, 2010.

[34]   N. Lassau, A. Spatz, and M. F. Avril, "Value of high frequency US for preoperative assessment of skin tumors," *Radiographics*, vol. 17, pp. 1559–1565, 1997.

[35]   S. Seidenari, "High-frequency sonography combined with image analysis: A noninvasive objective method for skin evaluation and description," *Clin. Dermatol.*, vol. 13, no. 4, pp. 349–359, 1995.

[36]   M. Nassiri-Kashani *et al.*, "Pre-operative assessment of basal cell carcinoma dimensions using high frequency ultrasonography and its correlation with histopathology," *Ski. Res. Technol.*, vol. 19, no. 1, pp. 132–138, 2013.

[37]   E. D. O. Barcaui and P. M. N. Valiante, "High-frequency ultrasound associated with

dermoscopy in pre-operative evaluation of basal cell carcinoma," pp. 828–831.

[38]   R. Kleinerman, T. B. Whang, R. L. Bard, and E. S. Marmur, "Ultrasound in dermatology: Principles and applications," *J. Am. Acad. Dermatol.*, vol. 67, no. 3, pp. 478–487, 2012.

[39]   J. Trumpaitis, R. Jurkonis, I. S. Akalauskaitė, and A. Paunksnis, "Application of Ultrasound Spectral Analysis for Choroidal Melanomas Before and After Treatment Analysis," *Balt. J. Mod. Comput.*, vol. 3, no. 1, pp. 55–71, 2015.

[40]   C. M. Moran, N. L. Bush, and J. C. Bamber, "Ultrasonic propagation properties of excised human skin," *Ultrasound Med. Biol.*, vol. 21, no. 9, pp. 1177–1190, 1995.

[41]   S. L. Bridal, C. Fournier, A. Coron, I. Leguerney, and P. Laugier, "Ultrasonic backscatter and attenuation (11-27 MHz) variation with collagen fiber distribution in ex vivo human dermis," *Ultrason. Imaging*, vol. 28, no. 1, pp. 23–40, 2006.

[42]   B. I. Raju, K. J. Swindells, S. Gonzalez, and M. A. Srinivasan, "Quantitative ultrasonic methods for characterization of skin lesions in vivo," *Ultrasound Med. Biol.*, vol. 29, no. 6, pp. 825–838, 2003.

[43]   S. Brand, E. C. Weiss, R. M. Lemor, and M. C. Kolios, "High Frequency Ultrasound Tissue Characterization and Acoustic Microscopy of Intracellular Changes," *Ultrasound Med. Biol.*, vol. 34, no. 9, pp. 1396–1407, 2008.

[44]   C. M. Botar-Jid *et al.*, "Assessment of cutaneous melanoma by use of very-high-frequency ultrasound and real-time elastography," *Am. J. Roentgenol.*, vol. 206, no. 4, pp. 699–704, 2016.

[45] M. C. Pierce, J. Strasswimmer, B. H. Park, B. Cense, and J. F. De Boer, "Advances in optical coherence tomography imaging for dermatology," *J. Invest. Dermatol.*, vol. 123, no. 3, pp. 458–463, 2004.

[46] J. Welzel, "Optical coherence tomography," in *Bioengineering of the skin: skin imaging and analysis*, Second., Germany: CRC Press, 2006, pp. 127–136.

[47] J. Welzel, M. Bruhns, and H. H. Wolff, "Optical coherence tomography in contact dermatitis and psoriasis," *Arch. Dermatol. Res.*, vol. 295, no. 2, pp. 50–55, 2003.

[48] M. Mogensen, L. Thrane, T. M. Joergensen, P. E. Andersen, and G. B. E. Jemec, "Optical Coherence Tomography for Imaging of Skin and Skin Diseases," *Semin. Cutan. Med. Surg.*, vol. 28, no. 3, pp. 196–202, 2009.

[49] J. Welzel, E. Lankenau, R. Birngruber, and R. Engelhardt, "Optical coherence tomography of the human skin.pdf," *Am. Acad. Dermatology*, vol. 37, no. 6, pp. 958–963, 1997.

[50] Y. Pan, E. Lankenau, J. Welzel, R. Birngruber, and R. Engelhardt, "Optical Coherence_Gated imaging of Biological Tissues.pdf," *IEEE J. Sel. Top. Electron.*, vol. 2, no. 4, pp. 1029–1034, 1996.

[51] T. Gambichler, R. Matip, G. Moussa, P. Altmeyer, and K. Hoffmann, "In vivo data of epidermal thickness evaluated by optical coherence tomography: Effects of age, gender, skin type, and anatomic site," *J. Dermatol. Sci.*, vol. 44, no. 3, pp. 145–152, 2006.

[52] N. D. Gladkova *et al.*, "In vivo optical coherence tomography imaging of human

skin: norm and pathology," *Ski. Res. Technol.*, vol. 6, no. 1, pp. 6–16, 2000.

[53]   R. Hospital and R. Hospital, "Assessment of Optical Coherence Tomography Imaging in the Diagnosis of Non-Melanoma Skin Cancer and Benign Lesions Versus Normal Skin: Observer-Blinded Evaluation by Dermatologists and Pathologists," pp. 965–972, 2009.

[54]   L. Themstrup, C. A. Banzhaf, M. Mogensen, and G. B. E. Jemec, "Optical coherence tomography imaging of non-melanoma skin cancer undergoing photodynamic therapy reveals subclinical residual lesions," *Photodiagnosis Photodyn. Ther.*, vol. 11, no. 1, pp. 7–12, 2014.

[55]   N. S. Claxton, T. J. Fellers, and M. W. Davidson, *Confocal Laser Scanning Microscopy*, vol. 1979, no. 21. 1979.

[56]   M. Rajadhyaksha, S. González, J. M. Zavislan, R. R. Anderson, and R. H. Webb, "In vivo confocal scanning laser microscopy of human skin II: Advances in instrumentation and comparison with histology," *J. Invest. Dermatol.*, vol. 113, no. 3, pp. 293–303, 1999.

[57]   R. F. Guthoff, A. Zhivov, and O. Stachs, "In vivo confocal microscopy, an inner vision of the cornea - A major review," *Clin. Exp. Ophthalmol.*, vol. 37, no. 1, pp. 100–117, 2009.

[58]   A. Nwaneshiudu, C. Kuschal, F. H. Sakamoto, R. Rox Anderson, K. Schwarzenberger, and R. C. Young, "Introduction to confocal microscopy," *J. Invest. Dermatol.*, vol. 132, no. 12, pp. 1–5, 2012.

[59]   M. Rajadhyaksha, M. Grossman, D. Esterowitz, R. H. Webb, and R. R. Anderson, "In vivo confocal scanning laser microscopy of human skin: Melanin provides strong contrast," *J. Invest. Dermatol.*, vol. 104, no. 6, pp. 946–952, 1995.

[60]   B. R. Masters, G. Gonnord, and P. Corcuff, "Three-dimensional microscopic biopsy of in vivo human skin: A new technique based on a flexible confocal microscope," *J. Microsc.*, vol. 185, no. March, pp. 329–338, 1997.

[61]   A. Gerger *et al.*, "Diagnostic applicability of in vivo confocal laser scanning microscopy in melanocytic skin tumors," *J. Invest. Dermatol.*, vol. 124, no. 3, pp. 493–498, 2005.

[62]   S. J. Edwards, G. Osei-Assibey, R. Patalay, V. Wakefield, and C. Karner, "Diagnostic accuracy of reflectance confocal microscopy using VivaScope for detecting and monitoring skin lesions: a systematic review," *Clin. Exp. Dermatol.*, vol. 42, no. 3, pp. 266–275, 2017.

[63]   G. Pellacani, A. M. Cesinaro, and S. Seidenari, "Reflectance-mode confocal microscopy of pigmented skin lesions-improvement in melanoma diagnostic specificity," *J. Am. Acad. Dermatol.*, vol. 53, no. 6, pp. 979–985, 2005.

[64]   M. Ulrich, E. Stockfleth, J. Roewert-Huber, and S. Astner, "Noninvasive diagnostic tools for nonmelanoma skin cancer," *Br. J. Dermatol.*, vol. 157, no. SUPPL. 2, pp. 56–58, 2007.

[65]   A. Gerger *et al.*, "Sensitivity and specificity of confocal laser-scanning microscopy for in vivo diagnosis of malignant skin tumors," *Cancer*, vol. 107, no. 1, pp. 193–

200, 2006.

[66] J. K. Barral, N. K. Bangerter, B. S. Hu, and D. G. Nishimura, "In vivo high-resolution magnetic resonance skin imaging at 1.5 T and 3 T," *Magn. Reson. Med.*, vol. 63, no. 3, pp. 790–795, 2010.

[67] L. Smith and S. MacNeil, "State of the art in non-invasive imaging of cutaneous melanoma," *Ski. Res. Technol.*, vol. 17, no. 3, pp. 257–269, 2011.

[68] B. Querleux, "Magnetic resonance imaging and spectroscopy of skin and subcutis," *J. Cosmet. Dermatol.*, pp. 156–161, 2004.

[69] H. Gufler, F. E. Franke, and W. S. Rau, "High-resolution MRI of basal cell carcinomas of the face using a microscopy coil.," *AJR. Am. J. Roentgenol.*, vol. 188, no. 5, pp. 480–484, 2007.

[70] M. R. Rajeswari *et al.*, "Evaluation of Skin Tumors by Magnetic Resonance Imaging," *Lab Investig.*, vol. 83, no. 9, pp. 1279–1283, 2003.

[71] G. Pennasilico, P. Arcuri, and F. Laschena, "Magnetic resonance imaging in the diagnosis of melanoma: in vivo preliminary studies with dynamic contrast-enhanced subtraction," *Melanoma*, vol. 12, pp. 365–371, 2002.

[72] D. Doroski, B. R. Tittmann, and C. Miyasaka, "Study of biomedical specimens using scanning acoustic microsocpy," in *Acoustical Imaging*, Volume 28., Michael P. Andre, Ed. San Diego, Califoronia: Springer, 2007, pp. 26–33.

[73] R. A. Lemons and C. F. Quate, "Acoustic microscope - Scanning version," *Appl. Phys. Lett.*, vol. 24, no. 4, pp. 163–165, 1974.

[74] R. G. Maev, *Acoustic Microscopy: Fundamentals and Applications*. 2009.

[75] E. Maeva, F. Severin, C. Miyasaka, B. R. Tittmann, and R. G. Maev, "Acoustic imaging of thick biological tissue," *IEEE Trans. Ultrason. Ferroelectr. Freq. Control*, vol. 56, no. 7, pp. 1352–1358, 2009.

[76] Y. Sayjo, M. Tanaka, H. Okawai, H. Sasaki, S.-I. Nitta, and F. Dunn, "Ultrasonic tissue characterization of infarcted myocardium by scanning acoustic micrsocopy," *Medicine (Baltimore).*, vol. 23, no. 1, pp. 77–85, 1997.

[77] T. Yamaguchi *et al.*, "Acoustic characteristics of fatty and fibrotic liver measured by an 80-MHz and 250 MHz scanning acoustic microscopy," *IEEE Int. Ultrason. Symp. IUS*, pp. 393–396, 2013.

[78] K. Miura and S. Yamamoto, "Histological Imaging of Gastric Tumors by Scanning Acoustic Microscope," vol. 4, no. 1, pp. 1–17, 2014.

[79] Y. Saijo, M. Tanaka, H. Okawai, H. Sasaki, S. I. Nitta, and F. Dunn, "Ultrasonic tissue characterization of photodamaged skin by scanning aocutsic microscopy," *Tokai J Exp Clin Med.*, vol. 30, no. 4, pp. 217–225, 2005.

[80] K. Miura, H. Nasu, and S. Yamamoto, "Scanning acoustic microscopy for characterization of neoplastic and inflammatory lesions of lymph nodes," *Sci. Rep.*, vol. 3, pp. 1–10, 2013.

[81] H. Sasaki1, Y. Saijo1, M. Tanaka1, S. Nitta1, T. Yambe1, and Y. Terasawa1, "Characterization of Renal Angiomyolipoma by Scanning Acoustic Microscopy," *J. Pathol.*, vol. 181, pp. 455–461, 1997.

[82] I. Bruno, R. E. Kumon, B. Heartwell, and E. Maeva, "Ex Vivo Breast Tissue Imaging and Characterization Using Acoustic Microscopy," pp. 279–287, 2007.

[83] M. N. Fadhel, E. S. L. Berndl, E. M. Strohm, and M. C. Kolios, "High-Frequency Acoustic Impedance Imaging of Cancer Cells," *Ultrasound Med. Biol.*, vol. 41, no. 10, pp. 2700–2713, 2015.

[84] S. Yoshida *et al.*, "Visualization of cancer distribution for living tissues using acoustic impedance microscope," *IEEE Int. Ultrason. Symp. IUS*, pp. 2014–2017, 2013.

[85] K. Miura and S. Yamamoto, "A scanning acoustic microscope discriminates cancer cells in fluid," *Sci. Rep.*, vol. 5, pp. 1–11, 2015.

[86] E. Weiss, P. Anastasiadis, G. Pilarczyk, R. Lemor, and P. Zinin, "Mechanical Properties of Single Cells by High-Frequency Time-Resolved Acoustic Microscopy," *IEEE Trans. Ultrason. Ferroelectr. Freq. Control*, vol. 54, no. 11, pp. 2257–2271, 2007.

[87] A. I. Gunawan *et al.*, "Numerical analysis of acoustic impedance microscope utilizing acoustic lens transducer to examine cultured cells," *Ultrasonics*, vol. 63, pp. 102–110, 2015.

[88] B. R. Tittmann, C. Miyasaka, E. Maeva, and D. Shum, "Fine Mapping of Tissue Properties on Excised Samples of Melanoma and Skin Without the Need for Histological Staining," vol. 60, no. 2, pp. 320–331, 2013.

[89] E. M. Strohm, M. Pasternak, M. Mercado, M. Rui, M. C. Kolios, and G. J. Czarnota,

"A comparison of cellular ultrasonic properties during apoptosis and mitosis using acoustic microscopy," *Proc. - IEEE Ultrason. Symp.*, pp. 608–611, 2010.

[90] J. E. Olerud *et al.*, "Ultrasonic assessment of skin and wounds with the scanning laser acoustic microscope.," *J. Invest. Dermatol.*, vol. 88, no. 5, pp. 615–623, 1987.

[91] J. H. Cantrell Jr, R. E. Goans, and R. L. Roswell, "Acoustic impedance variations at burn–nonburn interfaces in porcine skin," *J. Acoust. Soc. Am.*, vol. 64, p. 731, 1978.

[92] Y. Saijo, "Three-dimensional Ultrasound Imaging of Regenerated Skin with High Frequency Ultrasound," pp. 1231–1234, 2008.

[93] K. Kumagai *et al.*, "Imaging of sebaceous glands of human skin by three-dimensional ultrasound microscopy and its relation to elasticity," *Proc. Annu. Int. Conf. IEEE Eng. Med. Biol. Soc. EMBS*, pp. 7199–7202, 2011.

[94] K. Kumagai, H. Koike, R. Nagaoka, S. Sakai, K. Kobayashi, and Y. Saijo, "High-Resolution Ultrasound Imaging of Human Skin In Vivo by Using Three-Dimensional Ultrasound Microscopy," *Ultrasound Med. Biol.*, vol. 38, no. 10, pp. 1833–1838, 2012.

[95] Y. Saijo, K. Kobayashi, N. Hozumi, A. Tanaka, and S. Sakai, "Visualization of Microvessels in Skin by Three dimensional Ultrasound Microsocpe," *Acoust. Imaging*, vol. 30, pp. 107–112, 2011.

[96] R. J. Barr, G. M. White, J. P. Jones, L. B. Shaw, and P. A. Ross, "Scanning acoustic microscopy of neoplastic and inflammatory cutaneous tissue specimens," *J. Invest. Dermatol.*, vol. 96, no. 1, pp. 38–42, 1991.

[97] A. Briggs and O. Kolosov, *Acoustic Microscopy: Second Edition*, vol. 9780199232. 2010.

[98] Y. Saijo, "Acoustic microscopy — Beyond high resolution imaging," *2009 IEEE Int. Ultrason. Symp.*, pp. 37–40, 2009.

[99] J. Li, C. R. Friedrich, and R. S. Keynton, "Design and fabrication of a miniaturized, integrated high-frequency acoustical lens-transducer system," *J. Micromechanics Microengineering*, vol. 12, no. 3, pp. 219–228, 2002.

[100] M. D. Sherar and F. s. Foster, "the Design and Fabrication of High Frequency Polyvinylidene Fluoride Transducers," *Ultrason. Imaging*, vol. 11, no. 2, pp. 75–94, 1989.

[101] J. D. N. Cheeke, *Fundamentals and Applications of Ultrasonic waves*. Montreal, Qc: CRC Press, 2002.

[102] N. Hozumi *et al.*, "Time-frequency analysis for pulse driven ultrasonic microscopy for biological tissue characterization," *Ultrasonics*, vol. 42, no. 1–9, pp. 717–722, 2004.

[103] Y. Saijo, H. Sasaki, N. Hozumi, K. Kobayashi, M. Tanaka, and T. Yambe, "Sound speed scanning acoustic microscopy for biomedical applications," *Technol. Heal. Care*, vol. 13, no. 4, pp. 261–267, 2005.

[104] Y. Saijo, T. Miyakawa, H. Sasaki, M. Tanaka, and S. I. Nitta, "Acoustic properties of aortic aneurysm obtained with scanning acoustic microscopy," *Ultrasonics*, vol. 42, no. 1–9, pp. 695–698, 2004.

[105] X. Li, X. Xi, M. C, K. M, and T. BR, "High Frequency Scanning Acoustic Microscopy as Diagnostic Tool in Tissue Science," *J. Biotechnol. Biomater.*, vol. 3, no. 3, pp. 3–7, 2013.

[106] A. P. Sarvazyan, M. W. Urban, and J. F. Greenleaf, "Acoustic Waves in Medical Imaging and Diagnostics," *Ultrasound Med. Biol.*, vol. 39, no. 7, pp. 1133–1146, 2013.

[107] K. Kobayashi, S. Yoshida, Y. Saijo, and N. Hozumi, "Acoustic impedance microscopy for biological tissue characterization," *Ultrasonics*, vol. 54, no. 7, pp. 1922–1928, 2014.

[108] N. Hozumi, S. Kajima, A. I. Gunawan, and S. Yoshida, "Viscoelastic Imaging Using Acoustic Impedance Microscope and Its Application to Biological Tissue," pp. 3–6, 2015.

[109] Y. Saijo *et al.*, "Ultrasound speed and impedance microscopy for in vivo imaging," *Annu. Int. Conf. IEEE Eng. Med. Biol. - Proc.*, pp. 1350–1353, 2007.

[110] M. Arakawa, H. Kanai, K. Ishikawa, R. Nagaoka, K. Kobayashi, and Y. Saijo, "A method for the design of ultrasonic devices for scanning acoustic microscopy using impulsive signals," *Ultrasonics*, vol. 84, pp. 172–179, 2018.

[111] A. Atalar, "An angular-spectrum approach to contrast in reflection acoustic microscopy," *J. Appl. Phys.*, vol. 49, no. 10, pp. 5130–5139, 1978.

[112] T. Tarnoczy, "Sound focussing lenses and waveguides," *Ultrasonics*, vol. 3, no. 3, pp. 115–127, 1965.

[113] N. Hozumi *et al.*, "Development of biological acoustic impedance microscope and its error estimation," vol. 22, no. 11, pp. 1129–1135, 2008.

[114] E. Stockfleth, T. Rosen, and S. Shumack, "Histopathology of Skin Cancer," in *Managing skin cancer*, 2010, pp. 1–226.

[115] M. Lekka *et al.*, "Cancer cell detection in tissue sections using AFM," *Arch. Biochem. Biophys.*, vol. 518, no. 2, pp. 151–156, 2012.

[116] K. Hayashi and M. Iwata, "Stiffness of cancer cells measured with an AFM indentation method," *J. Mech. Behav. Biomed. Mater.*, vol. 49, pp. 105–111, 2015.

[117] M. Lekka, "Atomic Force Microscopy a Tip for Diagnosing cancer," *Nat. Publ. Gr.*, vol. 7, no. 11, pp. 691–692, 2012.

[118] M. Plodinec *et al.*, "The nanomechanical signature of breast cancer," *Nat. Nanotechnol.*, vol. 7, no. 11, pp. 757–765, 2012.

[119] L. R. Taggart, R. E. Baddour, A. Giles, G. J. Czarnota, and M. C. Kolios, "Ultrasonic characterization of whole cells and isolated nuclei," *Ultrasound Med. Biol.*, vol. 33, no. 3, pp. 389–401, 2007.

[120] T. Watanabe *et al.*, "Higher cell stiffness indicating lower metastatic potential in B16 melanoma cell variants and in (2)-epigallocatechin gallate-treated cells," *J. Cancer Res. Clin. Oncol.*, vol. 138, no. 5, pp. 859–866, 2012.

[121] G. Weder *et al.*, "Increased plasticity of the stiffness of melanoma cells correlates with their acquisition of metastatic properties," *Nanomedicine Nanotechnology, Biol. Med.*, vol. 10, no. 1, pp. 141–148, 2014.

[122] M. Sarna, A. Zadlo, B. Czuba-Pelech, and K. Urbanska, "Nanomechanical phenotype of melanoma cells depends solely on the amount of endogenous pigment in the cells," *Int. J. Mol. Sci.*, vol. 19, no. 2, 2018.

[123] B. Dasgeb, M. A. Morris, D. Mehregan, and E. L. Siegel, "Quantified ultrasound elastography in the assessment of cutaneous carcinoma," *Br. J. Radiol.*, vol. 88, no. 1054, pp. 19–21, 2015.

[124] X. Liang, "Biomechanical Properties of In Vivo Human Skin From Dynamic Optical Coherence Elastography," *IEEE Trans Biomed Eng.*, vol. 57, no. 4, pp. 953–959, 2013.

[125] A. Kimura *et al.*, "Development of cerebella tissue of rat characterized by acoustic impedance microscope," *Proc. - IEEE Ultrason. Symp.*, vol. 1, pp. 1421–1424, 2006.

[126] E. Farkas, Z. G. Meszena, A. Toldy, and S. Matko, "Polymer Degradation and Stability," *Polym. Degrad. Stab.*, vol. 93, pp. 1205–1213, 2008.

[127] T. W. Chean, N. Hozumi, S. Yoshida, K. Kobayashi, and Y. Ogura, "Mutual conversion between B-mode image and acoustic impedance image," 2017.

VITA AUCTORIS

NAME: Sarah Youssef

PLACE OF BIRTH: Baraachit, Lebanon

YEAR OF BIRTH: 1990

EDUCATION: Lebanese University, Degree in General Physics,
                                       Beirut, Lebanon, 2011

                                       Lebanese University, M.Sc.1 Biomedical Physics,
                                       Beirut, Lebanon, 2012

                                       Lebanese University, M.Sc.2 Biomedical Engineering
                                       in Medical Imaging, Beirut, Lebanon, 2013

                                       University of Windsor, M.Sc. Physics, Windsor, ON,
                                       2018